Significant Influence of the Boreal Summer Monsoon Flow on the Indian Ocean Response during Dipole Events

R. KRISHNAN AND P. SWAPNA

Indian Institute of Tropical Meteorology, Pune, India

(Manuscript received 3 August 2007, in final form 25 May 2009)

ABSTRACT

A majority of positive Indian Ocean dipole (IOD) events in the last 50 years were accompanied by enhanced summer monsoon circulation and above-normal precipitation over central-north India. Given that IODs peak during boreal autumn following the summer monsoon season, this study examines the role of the summer monsoon flow on the Indian Ocean (IO) response using a suite of ocean model experiments and supplementary data diagnostics. The present results indicate that, if the summer monsoon Hadley-type circulation strengthens during positive IOD events, then the strong off-equatorial southeasterly winds over the northern flanks of the intensified Australian high can effectively promote upwelling in the southeastern tropical Indian Ocean and amplify the zonal gradient of the IO heat content response. While it is noted that a strong monsoon cross-equatorial flow by itself may not generate a dipolelike response, a strengthening (weakening) of monsoon easterlies to the south of the equator during positive IOD events tends to reinforce (hinder) the zonal gradient of the upper-ocean heat content response. The findings show that an intensification of monsoonal winds during positive IOD periods produces nonlinear amplification of easterly wind stress anomalies to the south of the equator because of the nonlinear dependence of wind stress on wind speed. It is noted that such an off-equatorial intensification of easterlies over the SH enhances upwelling in the eastern IO off Sumatra–Java, and the thermocline shoaling provides a zonal pressure gradient, which drives anomalous eastward equatorial undercurrents (EUC) in the subsurface. Furthermore, the combination of positive IOD and stronger-than-normal monsoonal flow favors intensification of shallow transient meridional overturning circulation in the eastern IO and enhances the feed of cold subsurface off-equatorial waters to the EUC.

1. Introduction

Progress in understanding ocean–atmosphere coupled interactions in the Indian Ocean (IO) environment, together with insights from the Indian Ocean dipole (IOD) phenomenon have established the importance of IO dynamics on the regional climate variability (e.g., Saji et al. 1999; Webster et al. 1999; Behera et al. 1999; Murtugudde et al. 2000; Xie et al. 2002; Gualdi et al. 2003; Black et al. 2003; Annamalai and Murtugudde 2004; Yamagata et al. 2004; Kripalani et al. 2005). The development of IOD events is strongly phase locked to the seasonal cycle, as the oceanic anomalies evolve through boreal summer and attain peak amplitude in autumn. Several studies have drawn attention to the role of IOD events in influencing the variability of the Indian summer monsoon rainfall (ISMR). Behera et al. (1999) pointed out that the anomalous moisture transport from the southeastern tropical Indian Ocean (SETIO) during IOD events is conducive for enhanced monsoon precipitation over the Bay of Bengal (BOB) and the Indo-Gangetic plains.

Gadgil et al. (2004) reported that the interannual variability of ISMR is significantly related to the equatorial Indian Ocean oscillation (EQUINOO), which is the atmospheric component of IOD and is represented as a normalized index of the near-equatorial surface zonal wind anomaly. Ashok et al. (2001, 2004) further noted that positive IOD events can counteract the effects of El Niño on the Indian monsoon and thereby alter the ISMR variability. For instance, the summer monsoon of 1997 is a good example that illustrates this point. During this period, the Indian Subcontinent experienced above-normal monsoon precipitation, despite the evolution of a very intense El Niño in the Pacific.

Corresponding author address: R. Krishnan, Climate and Global Modelling Division, Indian Institute of Tropical Meteorology, Pashan, NCL Post, Pune 411008, India.
E-mail: krish@tropmet.res.in

DOI: 10.1175/2009JCLI2176.1

TABLE 1. JJAS seasonal monsoon rainfall anomaly over central-north India (20°–30°N, 73°–90°E) for the positive IOD events during 1958–2007. The anomalies are expressed as percentage departure from normal. The precipitation data are based on the IMD gridded rainfall over India for the period 1951–2007 (see Rajeevan et al. 2006). The positive IOD events are based on the classification of Meyers et al. (2007), which covers events until 1999; while the recent events (2006, 2007) are from http://www.jamstec.go.jp/frcgc/research/d1/iod.

	Positive IOD	JJAS rainfall anomaly over central-north India
1	1961	+21.57%
2	1963	−0.81%
3	1967	+5.02%
4	1972	−19.18%
5	1977	+7.05%
6	1982	−12.12%
7	1983	+6.77%
8	1991	−8.31%
9	1994	+18.95%
10	1997	+5.00%
11	2006	+5.81%
12	2007	+6.63%

Slingo and Annamalai (2000) showed that the strong suppression of convection over the equatorial eastern IO (EEIO) and the Maritime Continent during 1997 played a key role in altering the local monsoon Hadley circulation in a manner as to favor above-normal precipitation over India.

The period (1958–2007) witnessed 12 positive IOD events during 1961, 1963, 1967, 1972, 1977, 1982, 1983, 1991, 1994, 1997, 2006, and 2007 (Meyers et al. 2007); out of which the following 8 events—1961, 1967, 1977, 1983, 1994, 1997, 2006, and 2007—were accompanied by significant increase of seasonal monsoon rains over central-north India (see Table 1). For these 8 cases, the area-averaged rainfall over 20°–30°N, 73°–90°E for the June–September (JJAS) monsoon season exceeded the long-term normal by at least +5% (Table 1). Composite maps of SST, wind, and rainfall anomalies based on the 8 events (Fig. 1)[1] reveal anomalous SST cooling in the SETIO and warming in the west-central Indian Ocean (WIO), with accompanying southeasterly anomalies off Sumatra–Java and a patch of near-equatorial easterly anomalies. A striking feature in Fig. 1a is the

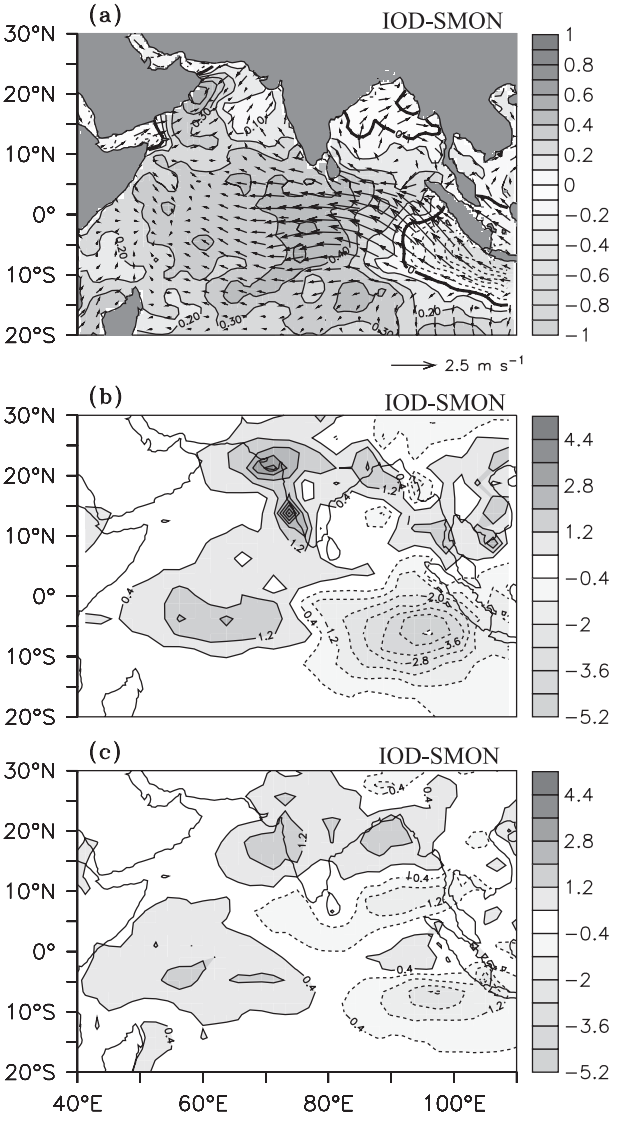

FIG. 1. Anomaly composite maps during IOD events: (a) SST (°C) and surface winds (m s^{-1}), (b) CMAP rainfall (mm day^{-1}), and (c) NCEP reanalysis rainfall for the JJAS monsoon season. The composites of SST, surface wind, and NCEP rainfall are based on the 8 IOD events (1961, 1967, 1977, 1983, 1994, 1997, 2006, and 2007) that were accompanied by above-normal monsoon precipitation (≥+5% departure) over central-north India (20°–30°N, 73°–90°E)—see Table 1. Since the CMAP rainfall dataset is available from 1979 onward, the composite of the CMAP rainfall anomaly is based on the years 1983, 1994, 1997, 2006, and 2007.

strengthened summer monsoon low-level flow characterized by anomalous southwesterlies to the north of 10°N over BOB and Arabian Sea and enhancement of monsoon precipitation over the Indian landmass and BOB (Figs. 1b,c). Studies have shown that rainfall enhancement over the Western Ghats can occur in response to increased evaporation by warm SST anomalies in the western IO and moisture transport toward the west

[1] Note that the rainfall composite in Fig. 1b is based on 5 IOD events (1983, 1994, 1997, 2006, and 2007) since the CMAP data are available during post-1979. Therefore, we have additionally shown the rainfall anomaly composite from NCEP reanalysis based on the 8 IOD events (Fig. 1c). Also we have separately shown in Fig. 3a the rainfall anomaly over the Indian land region composited from the 8 IOD events using the gridded rainfall data from IMD (see Rajeevan et al. 2006).

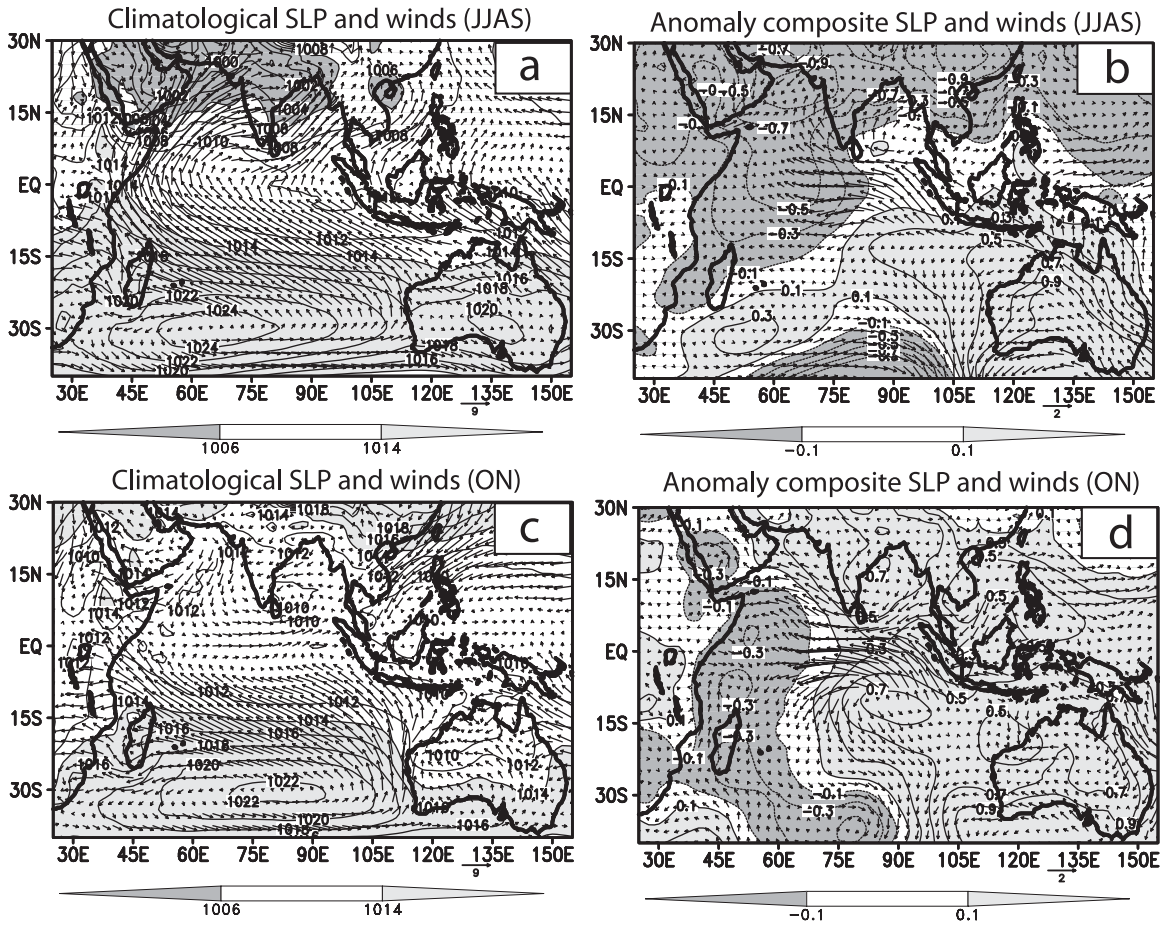

FIG. 2. Sea level pressure (hPa) and surface winds (m s^{-1}): (a) climatological mean for JJAS and (b) anomaly composites for JJAS based on the 8 IOD events (1961, 1967, 1977, 1983, 1994, 1997, 2006, and 2007). (c) Same as (a) except for ON months. (d) Same as (b) except for ON.

coast of India (e.g., Shukla 1975; Vecchi and Harrison 2004; Terray et al. 2007; Izumo et al. 2008).

A salient point to our discussion is the large-scale pattern of sea level pressure (SLP) and wind anomalies associated with the strong monsoonal flow conditions in Fig. 2b. The NH anomalous low is associated with a strengthened monsoon trough, while the SH high pressure anomalies correspond to an intensified Australian high (AH)—a semipermanent feature of the Asian summer monsoon system (Tao and Chen 1987). The anomalies are relative to the mean climatology (Figs. 2a,c). It is important to recognize that the off-equatorial easterly anomalies over SETIO during JJAS extend out to nearly 15°S over the northern flanks of the AH (Fig. 2b). The negative (positive) anomalies over the NH (SH) in Fig. 2b are indicative of the north–south gradient in the SLP anomaly. During October–November (ON), the easterly anomalies are predominantly seen over the equatorial region, with a pair of anticyclones straddling the equator. The prominent north–south contrast of the SLP and wind anomalies in the JJAS season (Fig. 2b) raises the question on the possible role of the anomalous monsoon off-equatorial winds in affecting the SETIO cooling during IOD episodes. The study of Drbohlav et al. (2007) showed that latent and sensible heat fluxes associated with a locally enhanced monsoon-type circulation contribute to the SETIO cooling more strongly than the WIO warming. While Drbohlav et al. (2007) mostly focused on oceanic mixed layer processes, the likely effects of an intensified monsoon flow on the IO subsurface dynamics remain to be resolved. Of particular interest are the transient equatorial undercurrents (EUC) in the IO, which feed the equatorial and Sumatra coastal upwelling during IOD events. It has been recently reported that the transient EUCs tend to be relatively stronger when IOD events co-occur with intensified summer monsoons (Swapna and Krishnan 2008). However, the physical mechanism through which the monsoonal wind forcing affects the EUC remains to be clarified.

The above discussions provide the rationale and impetus to gain deeper insight about the possible influence of summer monsoon flow intensification on the ocean response during IOD events. To clarify this issue, we have conducted a suite of simulations using a regional OGCM of the IO. In isolating the monsoonal flow effects, one needs to be aware of the relations among the Indian Ocean SST variability, ENSO, and the Indian monsoon (e.g., Lau and Nath 2000; Alexander et al. 2002; Annamalai et al. 2003; Feng and Meyers 2003; Saji et al. 2006; Drbohlav et al. 2007; Cherchi et al. 2007). Generally, El Niño (La Niña) events tend to favor deficit (excess) Indian summer monsoon rainfall (see http://www.tropmet.res.in), and they have mostly coincided with positive (negative) IOD events (see Meyers et al. 2007). Furthermore, ENSO events can influence IO SST anomalies via the ''atmospheric bridge'' (e.g., Lau and Nath 2000; Alexander et al. 2002). Therefore, while interpreting the monsoonal flow effects on dipole events, it is important to take into account the issue of monsoon interannual variability itself. Keeping this in view, we have designed the OGCM experiments by considering two categories of IOD events: those accompanied by (i) above-normal and (ii) below-normal summer monsoons (see section 2 for more details). Since the OGCM simulations of the observed IOD events alone may not be amenable to straightforward inferences, we have performed additional experiments using idealized wind forcing to facilitate better understanding of the IO dynamical response. Supplementary data diagnostics are included to strengthen the interpretation of results.

2. Datasets and OGCM

a. Datasets

The datasets used for diagnostics include surface winds from the National Centers for Environmental Prediction (NCEP) reanalysis during 1958–2007 (Kistler et al. 2001), SST from the Hadley Centre Sea Ice and Sea Surface Temperature dataset (HadISST1.1) (Rayner et al. 2003), and gridded rainfall from the India Meteorological Department (IMD) over India (Rajeevan et al. 2006) and from the Climate Prediction Center (CPC) Merged Analysis of Precipitation (CMAP) data (Xie and Arkin 1997) for the period 1979–2007. Additionally, the forcing for the OGCM simulations is computed using data of surface winds, net shortwave and longwave radiation, latent and sensible heat fluxes, precipitation, and evaporation from the NCEP reanalysis. We also use the Simple Ocean Data Assimilation (SODA) (Carton et al. 2000) products for analysis of oceanic fields. Because of lack of long-term subsurface observations, the SODA products away from the surface are largely an ocean model response to surface forcing in data-poor regions. Nevertheless, since the SODA products are consistent with the surface forcing specified from reanalysis, they at least provide tentative estimates of the upper-ocean circulation and variability.

b. OGCM details

The regional OGCM used here was developed at the Institute of Numerical Mathematics, Russia (Alekseev and Zalesny 1993). It is a sigma coordinate model and the domain covers the tropical IO (36°S–29.5°N, 22°–142°E) with horizontal resolution of 1° longitude × 0.5° latitude and uses realistic bottom topography and coastline. It has 33 unequal sigma levels in the vertical, of which 9 are in the upper 150 m. The model employs a Laplacian form of horizontal viscosity (viscosity coefficient = 2.0×10^7 cm^2 s^{-1}) and horizontal diffusion of heat and salt (diffusion coefficient = 1.5×10^7 cm^2 s^{-1}). The vertical mixing is based on a Richardson number–dependent scheme (Pacanowski and Philander 1981). The model numerics is based on the global version described by Diansky et al. (2002). Note that the present OGCM domain, which extends up to 142°E on the eastern side, includes much of the tropical west Pacific, and the model takes into account the influence of the exchange effects through the Indonesian straits by specifying the seasonal evolution of temperature and salinity at the liquid boundaries (Diansky et al. 2006). It may be mentioned that the global version of the OGCM was included as the ocean component in one of the coupled models of the Intergovernmental Panel on Climate Change's (IPCC) Fourth Assessment Report (Saji et al. 2006). To begin with, the OGCM was spun up to obtain quasi equilibrium. For this purpose, the model was initialized with climatological temperature and salinity from the *World Ocean Atlas* (http://www.nodc.noaa.gov/OC5/indprod.html) and integrated for 10 years. The climatological surface forcing for spinup was derived from NCEP reanalysis.

c. OGCM simulation experiments

Following the spinup, a suite of experiments were conducted using both observed and idealized wind forcing. The observed wind forcing experiments were performed with respect to (w.r.t.) the 8 IOD events (1961, 1967, 1977, 1983, 1994, 1997, 2006, and 2007), which were accompanied by strong monsoon conditions (Fig. 3a). For convenience, we refer to this set of IODs as IOD-SMON. We have also performed another set of experiments w.r.t. the positive IOD events (1972, 1982, and 1991), which co-occurred with weak monsoon conditions (see Table 1). The latter set is referred to as IOD-WMON. Notice that

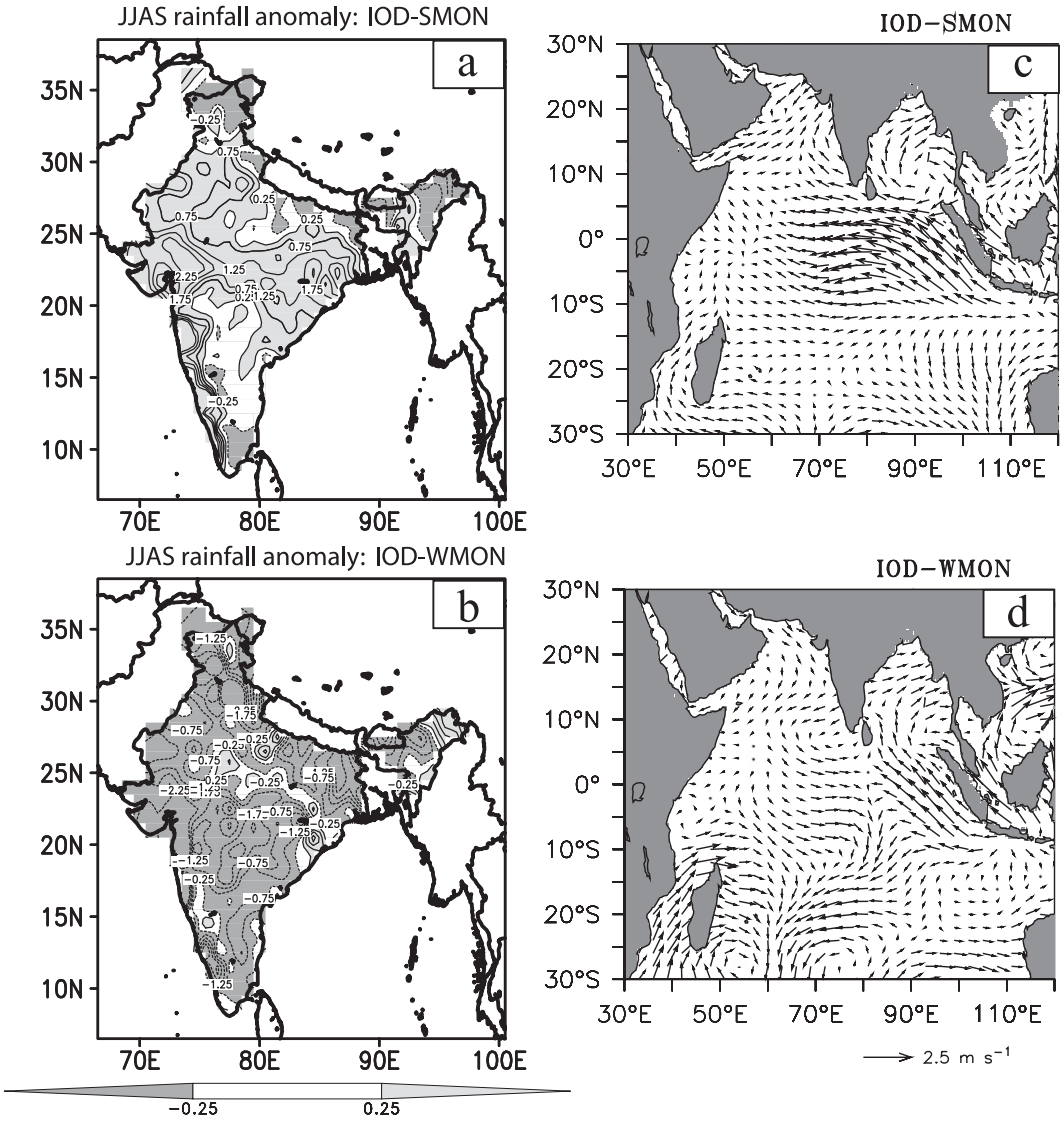

FIG. 3. Anomaly composites of JJAS rainfall (mm) over India based on the IMD gridded dataset for (a) IOD-SMON and (b) IOD-WMON. (c),(d) The corresponding surface wind anomaly composites are shown.

a majority of positive dipole events during (1958–2007) belong to the IOD-SMON category. It would have been desirable to have more cases for the IOD-WMON category as well. Nevertheless, this point should not really influence the overall analyses and interpretation of our results. To further strengthen our results, we have additionally backed up the observed wind forcing experiments (i.e., IOD-SMON and IOD-WMON) with idealized experiments that provide enhanced comprehension of the physical mechanisms relating to the influence of monsoonal wind forcing during IOD events.

The anomaly composites of summer monsoon rainfall over India in IOD-SMON and IOD-WMON are shown in Figs. 3a,b. The corresponding surface wind anomalies are shown in Figs. 3c,d. It can be noticed that the rainfall increase in IOD-SMON is largely over the west coast and central-north India to the south of the monsoon trough (Fig. 3a). The polarity of the precipitation anomalies is nearly reversed in the IOD-WMON case, which shows widespread rainfall deficit extending across most parts of India (Fig. 3b). The wind anomalies in IOD-SMON show strong southeasterlies off Sumatra, anomalous easterlies over equator and the SH subtropics, and an intensified monsoon cross-equatorial flow over the BOB and central-eastern Arabian Sea. In the IOD-WMON case, the southeasterly anomalies off Sumatra are much weaker, while anomalous westerlies can be seen near the equator around 60°–80°E. The weakened

summer monsoon flow is evident from the anomalous anticyclone over the Arabian Sea.

By comparing the IOD-SMON and IOD-WMON simulations, we shall deduce the influence of the monsoonal flow variations on the ocean response during positive IOD events. Since oceanic variations evolve much slower than those in the atmosphere, the OGCM simulations have been designed such that each IOD simulation has a long enough time span relative to that particular event. With this view, the model runs were initiated 1 year prior to an IOD episode and the integrations continued till the end of the following year for every IOD event. For example, the 1961 IOD simulation was based on the model run for the period January 1960 to December 1962; likewise the 1994 simulation covers the period January 1993 to December 1995. The theoretical justification for the above experimental design is that the time span of the model run for a particular IOD covers the wave adjustment time scales in the tropical IO Basin, which is predominantly characterized by circulations involving semiannual and annual components (Schott and McCreary 2001). Besides the observed IOD experiments, we have performed idealized simulations to gain deeper insight into the dynamical mechanisms.

3. Climatological seasonal cycle of the tropical Indian Ocean circulation

a. Mean features in SODA

Semiannual eastward currents in the equatorial IO during the spring and autumn monsoon transition periods known as Wyrtki jets (WJ) or equatorial jets are an important feature of IO circulation (Wyrtki 1973; Schott and McCreary 2001). The WJ transport warm waters to the EEIO and deepen the thermocline. The climatological thermocline depth, referenced by the 20°C isotherm depth (d20) (Murtugudde et al. 2000), is shown in Figs. 4a–c for the spring [March–May (MAM)], summer monsoon (JJAS), and autumn (ON), respectively. The WJ and the thermocline deepening in the EEIO (d20 $>$ 120 m) are clearly seen in MAM and ON. The current vectors have been averaged over the mixed layer (see figure caption). The deep thermocline in the EEIO is also evident from the longitude–depth section of temperature (Figs. 4d–f). The equatorial eastward currents are weaker in magnitude during the summer monsoon season, and the southwest monsoonal winds produce strong upwelling and thermocline shoaling off the coasts of Somalia and Arabia (see Schott 1983; Schott and McCreary 2001; Weller et al. 2002). In the south-central Arabian Sea (4°–12°N, 50°–65°E), a seasonal deepening (d20 $>$ 150 m) is seen during JJAS, which is consistent with earlier studies (e.g., Ramesh and Krishnan 2005). Between 5° and 12°S in the southern tropical IO, the d20 values are relatively shallower in the western side (~50°–75°E) and are associated with Ekman divergence caused by a cyclonic gyre (e.g., Reverdin et al. 1986; Molinari et al. 1990; Murtugudde et al. 1999; Xie et al. 2002; Yokoi et al. 2009; Hermes and Reason 2008). In this region, the negative wind curl between the southeasterly trades and equatorial westerlies raises the thermocline, leading to open-ocean upwelling (Xie et al. 2002). The shallow thermocline ridge in the southwest tropical IO is also known in the literature as the Seychelles Dome (Hermes and Reason 2008; Yokoi et al. 2009).

b. Mean features in the model simulation

The simulation shows the climatological eastward equatorial currents and thermocline deepening in the EEIO during MAM and ON (Fig. 5). The simulated d20 for JJAS shows a shallow thermocline off Somalia and Arabia and deepening in the south-central Arabian Sea. In noting the above features, we do realize some systematic model biases. For example, the simulated equatorial eastward currents have magnitudes ~30–40 cm s^{-1}, which are small compared to observed currents (see Masumoto et al. 2005; Lakshmi et al. 2007). Observations of the fall WJ at 77° and 83°E during 2004 and 2005 showed that the core of the WJ had speeds $>$ 70 cm^{-1} (Lakshmi et al. 2007). They also noted reduced speed of the WJ at the 93°E longitude as compared to those at 77° and 83°E. The deep d20 values ($>$120 m) extend considerably westward in the simulation so that the east–west slope of the equatorial d20 is somewhat weak in the model. The same has also been verified by comparing the model-simulated d20 with the World Ocean Circulation Experiment (WOCE) climatology (figure not shown). Nevertheless, these systematic model biases should not affect the overall thrust of our study for the following reasons. First, the evaluation of the IOD response in the model is performed relative to the model climatology. Second, the IPCC model assessment by Saji et al. (2006) showed that the global version of the OGCM had reasonable skill in capturing the IOD variability. We will revisit this point again later. Furthermore, the climatological annual cycle in the model simulation is fairly consistent with that of SODA. For example, the correlation coefficient (CC) between the model simulation and SODA for the climatological annual cycle of d20 in the eastern IO (10°S–5°N, 85°–100°E) is ~0.9. Likewise the climatological annual cycle of the model-simulated near-surface zonal currents in the equatorial eastern IO shows a CC ~0.98 with that of SODA.

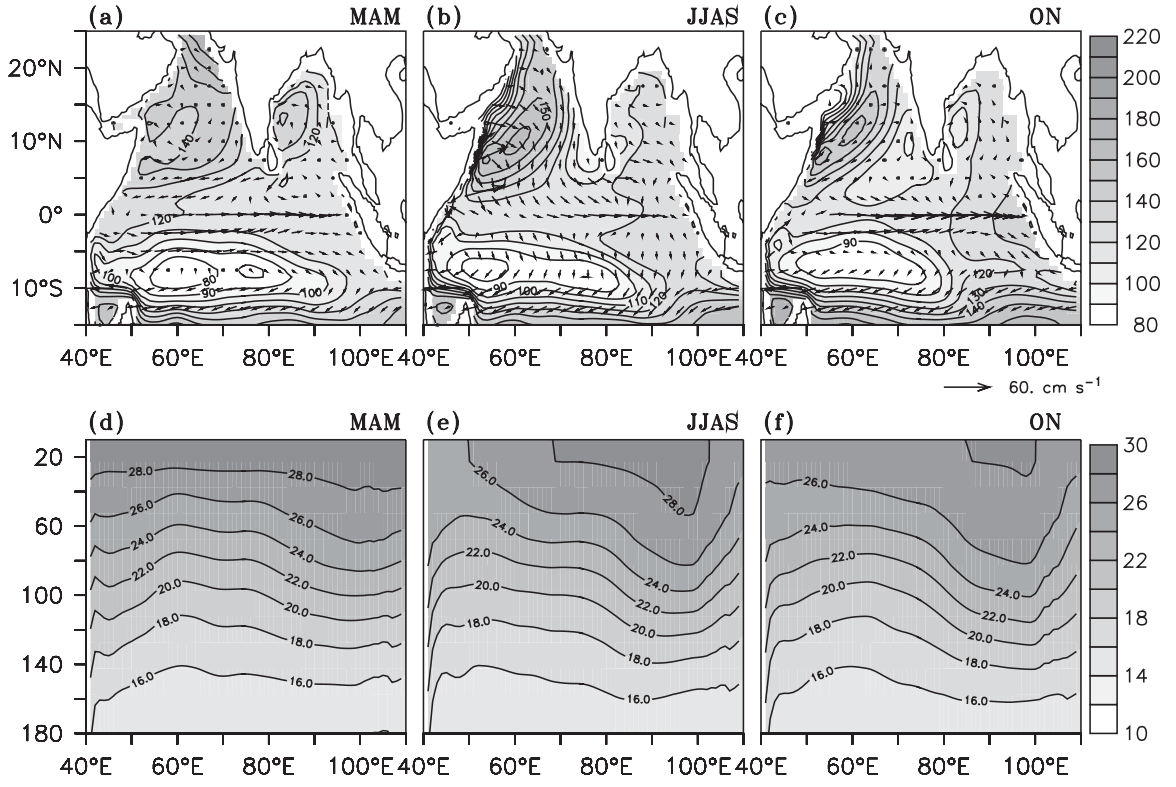

FIG. 4. Climatological seasonal cycle of d20 (m) and vertically averaged currents (cm s^{-1}) within the mixed layer: (a) MAM, (b) JJAS, and (c) ON. The mixed layer depth criterion selected is a threshold value of temperature from the near-surface value at 10-m depth ($\Delta T = 0.2$°C), which is based on de Boyer Montégut et al. (2004). Longitude–depth sections of temperature (°C) averaged between the equator and 10°S for (d) MAM, (e) JJAS, and (f) ON. The data are from SODA.

4. Observed and model-simulated IOD anomalies

a. Anomalies of d20, currents, and subsurface temperature

Composites of d20 and current anomalies from SODA are shown for the IOD-SMON and IOD-WMON cases in Fig. 6. Anomalous westward currents in the equatorial region are quite prominent in the IOD-SMON case during JJAS and ON (Figs. 6a,b). The negative d20 anomalies in the SETIO indicate an elevated thermocline associated with enhanced upwelling off Sumatra, while the positive d20 anomalies to the west indicate a deepened thermocline. For the IOD-WMON case, the thermocline shoaling in the SETIO and the westward current anomalies are much weaker as compared to IOD-SMON. Basically the zonal contrast in the d20 response is strongly manifested in IOD-SMON (Figs. 6a,b) as compared to the IOD-WMON case (Figs. 6c,d). The stronger thermocline shoaling and enhanced upwelling in the SETIO in the IOD-SMON case resulted in stronger subsurface cooling as compared to IOD-WMON (figures not shown). We computed the heat content anomalies in the upper 200 m of the eastern (10°S–equator, 85°–105°E) and western (10°S–equator, 45°–75°E) IO and examined the zonal contrast (east minus west difference) of the heat content anomalies. The east-to-west difference in heat content anomalies was found to be -0.81×10^9 J m^{-2} in IOD-SMON and -0.07×10^9 J m^{-2} in IOD-WMON. By performing a statistical t test, we have noted that the difference in the zonal gradient of heat content response between IOD-SMON and IOD-WMON is less than the 10% significance level. This suggests that the null hypothesis of insignificant difference in the zonal gradient of heat content response between IOD-SMON and IOD-WMON can be rejected with 90% confidence level.[2] Later in section 5e, we shall discuss the possible physical mechanisms through which the monsoonal wind forcing can influence the zonal gradient of the heat content anomalies during IOD events.

Figure 7 shows composites of d20 and current anomalies from the model simulation. For the IOD-SMON case (Figs. 7a,b), the simulation shows thermocline shoaling in the SETIO with d20 anomalies of ~−40 m.

[2] The number of degrees of freedom for the t test is ($N_{\text{IOD-SMON}} + N_{\text{IOD-WMON}} - 2$) = 9.

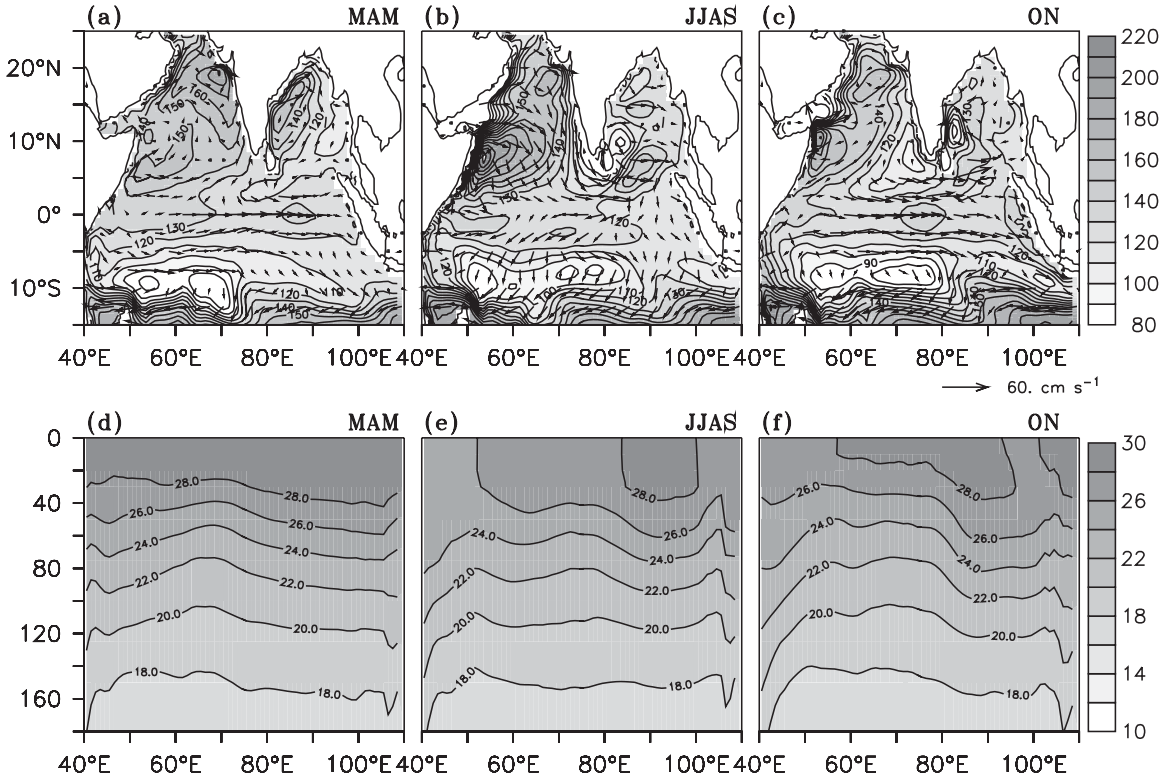

FIG. 5. Same as Fig. 4 except for OGCM.

Computations of the root-mean-square error (RMSE) of d20 anomalies in the eastern IO (10°S–5°N, 85°–100°E) between the model simulation and SODA indicated that the RMSE value was about 8 m.[3] Furthermore, the assessment of the IPCC climate simulations by Saji et al. (2006) showed that the global version of the present OGCM adequately captures the IOD-related variability of d20 and SST. The IOD-SMON simulation also shows anomalous equatorial westward currents extending to the west of 100°E during JJAS and ON; they are known to be forced by easterly winds (see Murtugudde et al. 2000; Vinayachandran et al. 2002; Feng et al. 2001; Rao et al. 2002). Current-meter moorings deployed in the equatorial IO during 1993–94 revealed surface currents with speeds >150 cm s^{-1} during September 1993 to January 1994, while the eastward flow was much weaker (~50 cm s^{-1}) during March until May/June 1994 (Reppin et al. 1999). The magnitude of the near-equatorial current anomalies in the IOD-SMON simulation around 70°–100°E for the JJAS and ON months is about 40 cm s^{-1} and compares with other simulations (e.g., Reppin et al. 1999; Vinayachandran et al. 1999). The important point to be noted here is that the d20 and westward current anomalies are relatively stronger in the IOD-SMON simulation as compared to the IOD-WMON counterpart. The simulations are also consistent in showing considerable enhancement of the zonal contrast of d20 anomalies in IOD-SMON as compared to IOD-WMON.

b. *Anomalous equatorial undercurrents*

An important observation during positive IOD periods is the occurrence of transient EUC. Current-meter moorings in the equatorial IO provided vital evidence for eastward EUC during the summer of 1994, with speeds >40 cm s^{-1} at depths of about 150 m (Reppin et al. 1999). More recently, Lakshmi et al. (2007) have reported eastward-flowing EUC during the 2006 IOD based on current measurements from acoustic Doppler current profiler (ADCP). In particular, their observations showed monsoon EUC at 83°E during mid-June and July 2006 in the depth range of 100–125 m having speeds between 25–50 cm s^{-1}. While the EUCs in the IO are regarded as transients driven by eastward pressure gradient force caused by prevailing easterlies (Schott and McCreary 2001), earlier studies have pointed that the EUCs can develop during IOD events and they play an important role in supplying subsurface

[3] Since there are 11 IOD cases and the model run for a particular IOD event covers a 3-yr period, the total sample size for the RMSE computation is 33.

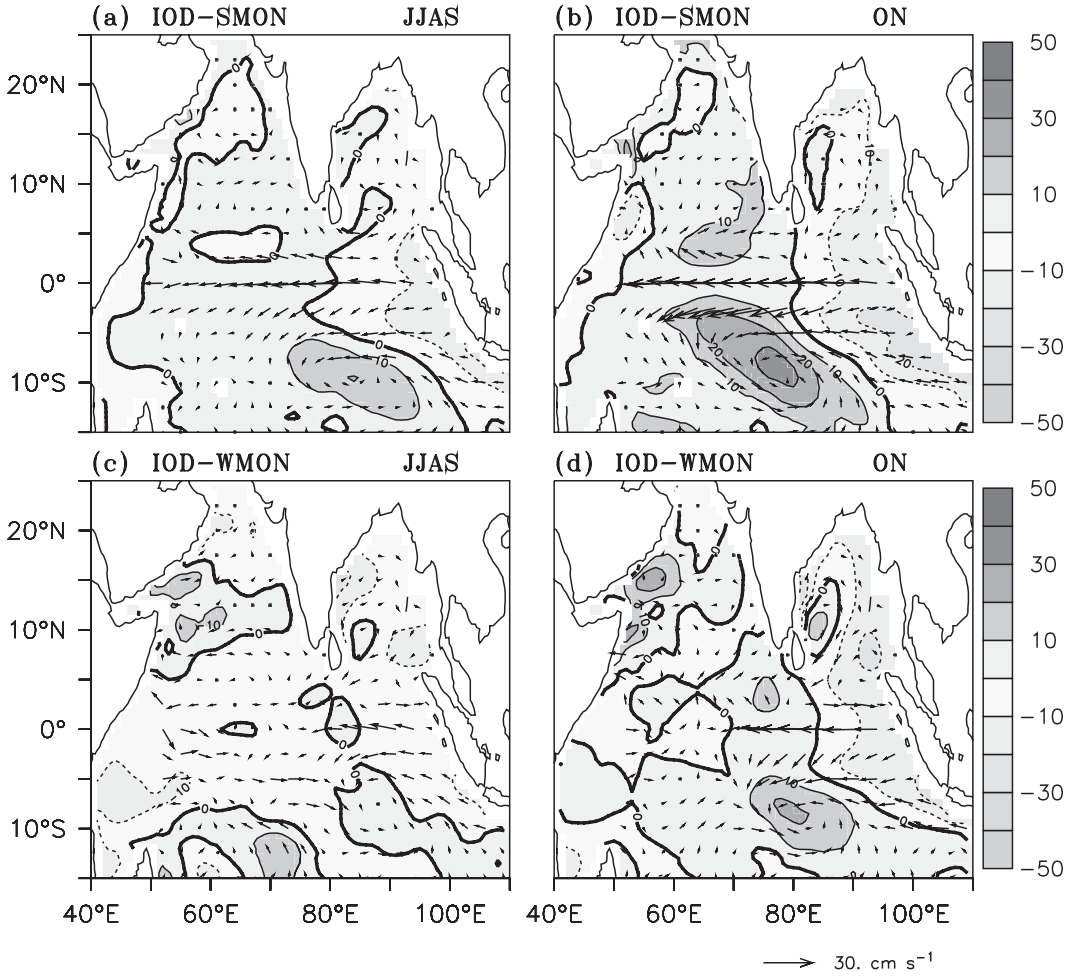

FIG. 6. Composite maps of d20 (m) and current (cm s^{-1}) anomalies based on the (a),(b) IOD-SMON and (c),(d) IOD-WMON cases. The anomaly composites are shown for the (left column) JJAS and (right column) ON seasons and the data are from SODA.

cool waters to the upwelling region in the eastern IO (Reppin et al. 1999; Vinayachandran et al. 1999).

In the Pacific and Atlantic Oceans, the EUC is a quasi-permanent eastward current at the top of the thermocline that is driven by the eastward pressure gradient force set up by the steady easterly trade winds (e.g., Stommel 1960; Philander and Pacanowski 1980; McCreary 1981, 1985; Pedlosky 1987). Also, the link between the equatorial zonal winds and the EUC has been extensively studied. The depth, speed, and mass transport of the Pacific EUCs show significant linear dependence on the equatorial zonal wind stress integrated longitudinally over its fetch from the eastern boundary of the basin westward (e.g., McPhaden 1993; Izumo 2005). In addition, the effects of nonlinear acceleration can be quite important for attaining high speeds of the EUCs (Wacongne 1990). The EUCs are fed by shallow meridional overturning cells, wherein the EUC cold waters come partly from the subduction regions in the subtropics (see Pedlosky 1987; McCreary and Lu 1994; Blanke and Raynaud 1997; Izumo 2005); the EUC waters are also fed by the tropical cells (e.g., Blanke and Raynaud 1997, Lu et al. 1998; Masson et al. 2004). Unlike the Pacific and Atlantic Oceans, the EUCs in the IO are transient in nature. Current-meter observations by Reppin et al. (1999) showed the presence of EUC in the equatorial IO during the summer of 1994, while the EUC was absent during the summer of 1993. Model simulation studies of the 1994 IOD event suggest that the shoaling of thermocline in the eastern IO provided the zonal pressure gradient along the equator for driving the eastward EUC (e.g., Reppin et al. 1999; Vinayachandran et al. 1999). Swapna and Krishnan (2008) have recently noted that the EUCs tend to be stronger when positive IOD events co-occur with intensified summer monsoon flows, as compared to dipole events co-occurring with weak monsoons.

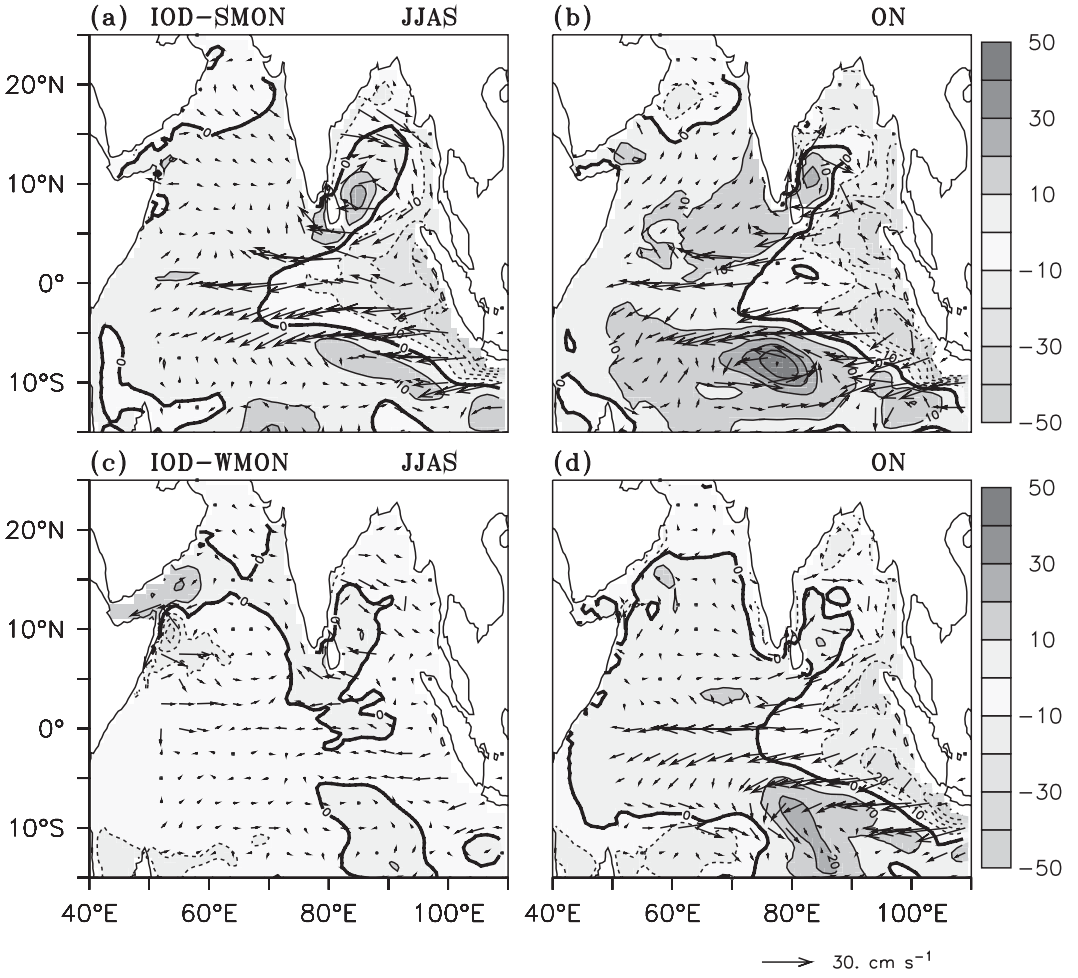

FIG. 7. Same as Fig. 6 except for OGCM.

Longitude–depth sections of zonal current anomalies are shown for the IOD-SMON and IOD-WMON cases in Fig. 8. The zonal current anomalies, averaged between 2°S and 2°N, are shown for the JJAS and ON seasons both from SODA and the OGCM simulation. In the IOD-SMON case, anomalous westward currents can be noticed in the near-surface layers together with EUC anomalies at depths ~100 m and below. The maximum EUC anomaly associated with the IOD-SMON is ~10–15 cm s^{-1} and located at a depth of about 90–100 m (Figs. 8a–d). The subsurface current anomalies show an east–west slope and exhibit an overall intensification from the summer monsoon (JJAS) through the fall (ON) season. This feature is associated with deepening of the westward near-surface current anomalies on the western side and upward sloping of the eastward EUC on the eastern side. In contrast, the IOD-WMON case shows weak westward current anomalies in the near-surface layers (Figs. 8e–h). Also it may be noted that the eastward EUC anomalies are very weak or nearly absent in the IOD-WMON case. The differences in the EUC anomalies between IOD-SMON and IOD-WMON are consistently reflected in the zonal pressure gradient at the subsurface. The longitudinal variation of pressure anomaly at 100 m depth, along the equator, is shown for the IOD-SMON and IOD-WMON experiments in Figs. 8i and 8j for the JJAS and ON months, respectively. In the IOD-SMON case, a significant drop in the subsurface pressure anomaly can be seen in the EEIO and the maximum drop is ~600–800 N m^{-2} around 95°E. Furthermore, an anomalous pressure rise of about 100 N m^{-2} can be seen near 60°E on the western side in IOD-SMON. In contrast for the IOD-WMON case, the pressure drop in the EEIO is very small and the zonal pressure gradient is considerably weaker as compared to IOD-SMON.

5. Dynamics of IO response to monsoon and IOD wind forcing

To gain further insight into the dynamics of the IO response, we have performed an additional suite of

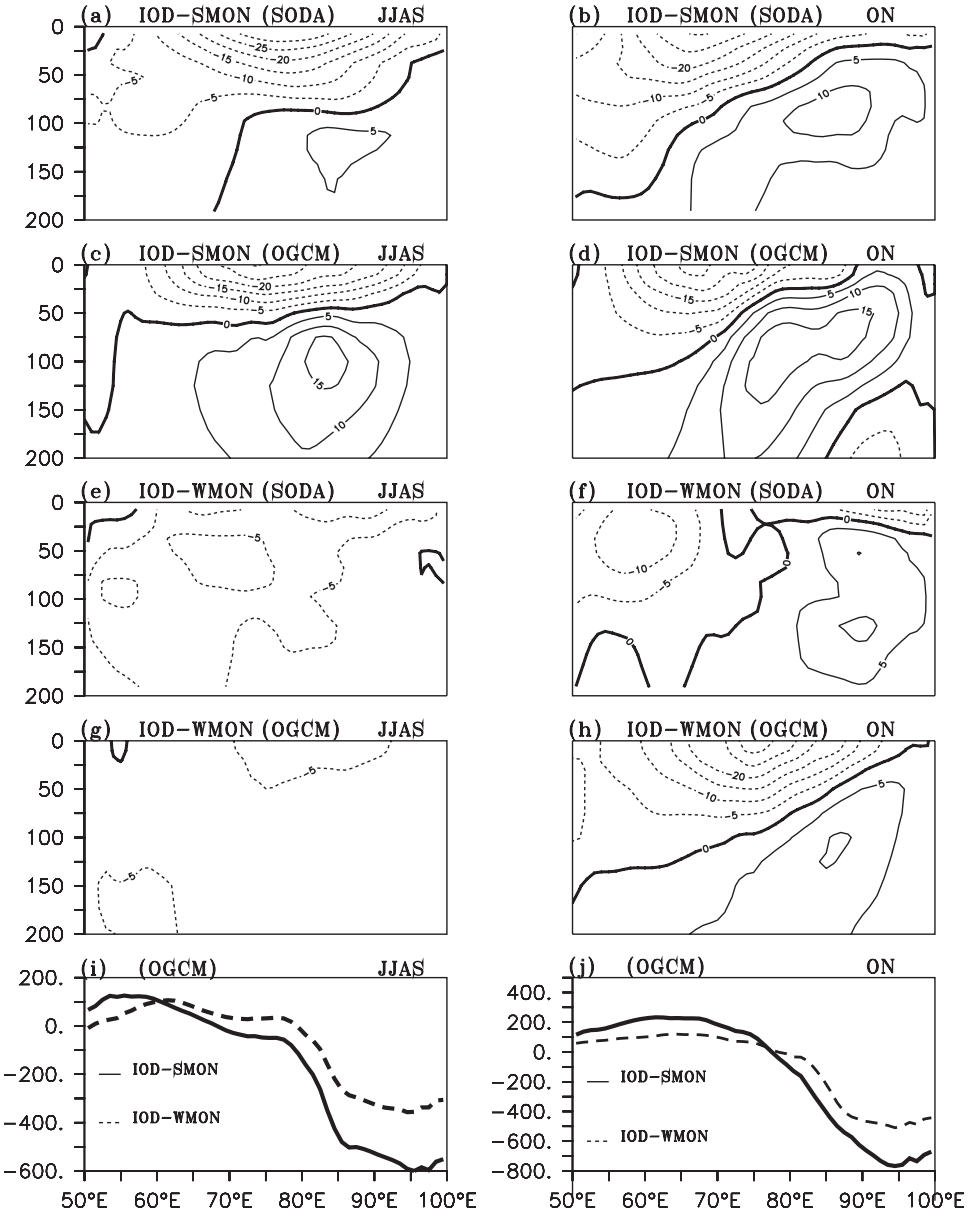

FIG. 8. (a)–(h) Longitude–depth sections show composite maps of zonal velocity anomalies (cm s^{-1}) for the IOD-SMON and IOD-WMON cases based on SODA and OGCM. (i)–(j) Longitudinal variation of pressure anomaly (N m^{-2}) averaged between 2°S and 2°N at 100 m for the IOD-SMON (solid line) and IOD-WMON (dashed line) simulations. The left (right) columns are for the JJAS (ON) seasons.

simulations forced by idealized winds that broadly mimic the structure of the large-scale circulation pattern associated with positive IOD and stronger-than-normal summer monsoon flow conditions. For this purpose, idealized wind anomalies were first generated using simplified patterns of atmospheric diabatic heating. The strategy for computing the idealized wind forcing is to determine idealized Gill-type wind response to a specified atmospheric diabatic-heating anomaly (Gill 1980). This is based on the premise that the wind anomalies during IOD events are closely related to the regional precipitation anomalies. It was earlier noticed that a majority of positive IOD events were associated with enhanced monsoon precipitation over central-north India occurring in conjunction with a dipole-type pattern of negative (positive) rainfall anomalies over the eastern (western) tropical IO (Figs. 1b,c and 3a). Rainfall anomalies in the tropics basically correspond to anomalies in the diabatic-heating field, with positive rainfall anomalies representing heat sources (i.e., largely release

of latent heat from moist convection) and negative anomalies representing heat sinks associated with radiative cooling (Gill 1980).

a. Gill-type monsoon wind forcing

In a pioneering work, Gill (1980) elucidated the basic dynamics of large-scale tropical circulation response to idealized heating. He showed that the large-scale summer monsoon flow broadly resembles a $n = 2$ planetary (Rossby) wave forced by an antisymmetric forcing w.r.t. the equator [i.e., heating (cooling) to the north (south) of equator described mathematically by (1) and (2)]. In the equations given below, (x, y) is nondimensional distance with x eastward and y measured northward from the equator. The nondimensional length and time scales are chosen as in Gill (1980). The nondimensional pressure perturbation (p), zonal wind (u), and meridional wind (v) response for the Gill-type monsoon are given by (3)–(5). Here, ε is the nondimensional damping from Rayleigh friction and Newtonian cooling, and 2L is the longitudinal width of the heating:

$$Q(x, y) = F(x)y\exp(-\frac{1}{4}y^2), \tag{1}$$

$$F(x) = \begin{cases} \cos(kx) & |x| < L \\ 0 & |x| > L \end{cases} \quad \text{where,} \quad k = \frac{\pi}{2L}. \tag{2}$$

Figure 9a shows the Gill-type monsoon wind and pressure anomaly (shading) generated by an idealized forcing that is antisymmetric w.r.t. the equator. The forcing is prescribed such that the idealized circulation response broadly mimics the intensified summer monsoon flow anomaly (see Fig. 2b). The idealized response was computed from (4)–(6) by setting $\varepsilon = 0.1$. The wind anomalies (Fig. 9a) show easterlies (westerlies) to the north (south) of equator. Also seen in Fig. 9a are the intensified monsoon trough and the AH and the off-equatorial easterly anomalies to the south of the equator:

$$p = \frac{1}{2}q_3(x)y^3\exp(-\frac{1}{4}y^2), \tag{3}$$

$$u = \frac{1}{2}q_3(x)(y^3 - 6y)\exp(-\frac{1}{4}y^2), \tag{4}$$

$$v = [6\varepsilon q_3(x)(y^2 - 1) + F(x)y^2]\exp(-\frac{1}{4}y^2), \tag{5}$$

where

$$\{25\varepsilon^2 + k^2\}q_3 = -k[1 + \exp\{-10\varepsilon L\}]\exp\{5\varepsilon(x + L)\} \quad \text{for} \quad x < -L \tag{6a}$$

$$\{25\varepsilon^2 + k^2\}q_3 = -5\varepsilon\cos kx + k[\sin kx - \exp\{5\varepsilon(x - L)\}] \quad \text{for} \quad |x| < L \tag{6b}$$

$$\{25\varepsilon^2 + k^2\}q_3 = 0 \quad \text{for} \quad x > L \tag{6c}$$

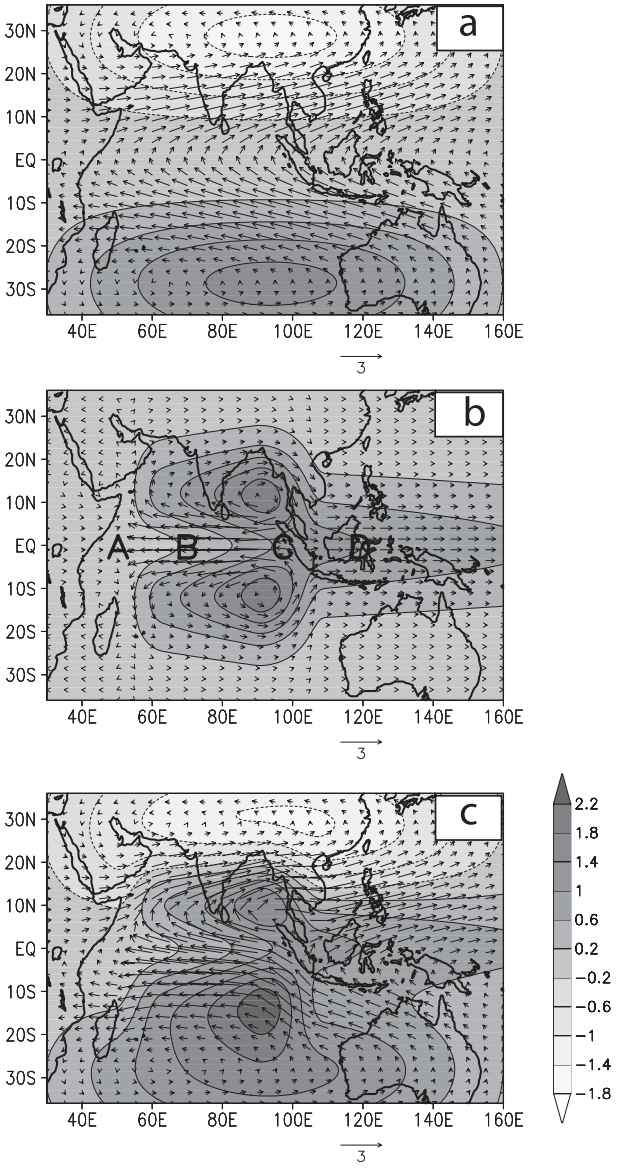

FIG. 9. Idealized wind vector anomalies (m s^{-1}) used to force the OGCM. The shaded field is the idealized pressure perturbation: (a) Gill-type monsoonal wind forcing, (b) idealized IOD forcing, and (c) Gill-type monsoon + idealized IOD wind forcing. Labels A, B and C, D in Fig. 9b indicate the approximate longitudinal extents of the idealized IOD heat source and heat sink, respectively. The idealized wind anomalies in the three experiments are constructed so as to broadly mimic the large-scale circulation anomalies during IOD events (see Figs. 2b,d).

In the first idealized experiment, we examined the OGCM response to the Gill-type monsoonal wind forcing. Given the seasonality of the southwest monsoon circulation (which starts in May, develops in June, peaks in July–August, withdraws in September, and later decays in October), we have prescribed a seasonal variation by providing weights to the wind forcing. Accordingly, the weights are set to zero during January–April and November–December, while the weights for May, June, July, August, September, and October are set to be 0.5, 0.75, 1.0, 1.0, 0.75, and 0.25, respectively. The Gill-type wind anomalies are multiplied by these weights (Fig. 9a). The amplitude-weighted wind anomalies are then superposed on the climatological surface winds to obtain the total wind field required for driving the OGCM.

b. Idealized IOD wind forcing

In the second experiment, the influence of an idealized IOD wind forcing on the IO response was examined. The wind forcing was constructed for a dipolelike idealized forcing consisting of a heat source in the WIO and a heat sink in the EEIO. For simplicity, the heat source and heat sink are assumed to be symmetric w.r.t. the equator. It can be seen from (7) and (8) that the heat source longitudinally lies between A and B and the heat sink between C and D. The points A and B are chosen as 54° and 68°E so that the maximum heating in the equatorial WIO is ~61°E. The points C and D are chosen as 100° and 120°E, so that the maximum cooling in the EEIO is ~110°E. The choice of a longer zonal extent of the heat sink as compared to that of the heat source is based on the pattern of precipitation anomaly (Fig. 1b), which shows a larger zonal extent of negative anomaly in the east as compared to that of the positive anomaly in the west. The effective latitudinal width of the heat source roughly extends between 15°S and 15°N, with maximum heating at the equator and decreases in magnitude away from the equator. The constant (H) in (8) is the nondimensional heating amplitude, which is set to unity:

$$Q(x, y) = F(x)\exp(-\frac{1}{4}y^2), \quad \text{where} \tag{7}$$

$$F(x) = \begin{cases} 0 & \text{if} \quad x \le A \\ H(x-A)(B-x) & \text{if} \quad A \le x \le B \\ 0 & \text{if} \quad B \le x \le C \\ -H(x-C)(D-x) & \text{if} \quad C \le x \le D \\ 0 & \text{if} \quad x \ge D \end{cases}. \tag{8}$$

Gill (1980) showed that the Kelvin ($n = 0$) and Rossby ($n = 1$) wave responses to a symmetric forcing w.r.t. the equator are given by

$$\frac{dq_0}{dx} + \varepsilon q_0 = -F(x), \tag{9}$$

$$\frac{dq_2}{dx} - 3\varepsilon q_2 = F(x). \tag{10}$$

In (9) and (10), the variable $q = u + p$ is the sum of the zonal wind and pressure perturbations. The solution to the above equations is obtained by following the treatment for first-order linear inhomogeneous equations (see Bender and Orszag 1978):

$$q_0(x) = \alpha\exp(-\varepsilon x) - \exp(-\varepsilon x)\int F(x)\exp(\varepsilon x)\,dx, \tag{11}$$

$$q_2(x) = \beta\exp(3\varepsilon x) + \exp(3\varepsilon x)\int F(x)\exp(-3\varepsilon x)\,dx. \tag{12}$$

The response within the forcing region consists of the free and the forced components. Outside the forcing region, the response consists of the free component alone. The integration constants α and β in (11) and (12) can be determined by matching the solution in different regions of the domain and by using cyclic boundary conditions (Krishnan 1993). Basically, the surface wind anomalies within the dipole region (61°–110°E) is composed of free Kelvin waves originating from the heat source and free Rossby waves from the heat sink. The combination of the free Kelvin and Rossby waves gives rise to strong easterly wind anomalies over the equatorial region (Fig. 9b). Notice that the idealized equatorial easterly wind anomalies exhibit zonal variations, with maximum amplitude occurring in the 50°–100°E longitude band.

c. Idealized (monsoon + IOD) wind forcing

The third experiment examines the IO response to the combined influence of an idealized IOD wind forcing and a Gill-type monsoon wind forcing (Fig. 9c), which is simply the sum of wind anomalies shown in Figs. 9a,b. The wind forcing for the third idealized experiment is constructed by superposing the combined wind anomaly (Fig. 9c) on the climatological wind field. As in the first idealized experiment, a seasonal variation has been prescribed in the combined wind forcing experiment for the Gill-type monsoon anomaly component but not for the idealized IOD component. The boreal summer monsoon circulation has a strong seasonal cycle and does not extend into late autumn months. Therefore, it is essential that a seasonal variation is prescribed for the monsoon wind forcing component. Although, we realize that the IOD wind forcing is also phase locked to the seasonal cycle, the prescription of seasonal variation to

both the monsoon and the IOD wind forcing components would render more complexity to the experiments. Moreover, our intention is to keep the design of the OGCM experiments as simple as possible, so that the interpretation of the monsoonal flow effects on the IO response during IOD events can be more straightforward and focused.

A striking feature in Fig. 9c is the belt of strong equatorial easterly anomalies between 50° and 110°E. The easterly anomalies are weaker to the west of 50°E, thus indicating a zonally varying wind forcing over the equatorial region. Notice that the easterly anomalies extend southward to about 20°S, while their meridional extent to the north of the equator is relatively small. Also the easterly anomalies to the south of the equator (10°S–equator, 75°–100°E) are relatively stronger in magnitude than their northern counterpart (equator–5°N, 75°–100°E). To the south of the equator, there is a reinforcement of easterlies from the Gill-type monsoon and the idealized IOD forcing, while to the north of the equator the monsoon westerly anomalies are opposite to the easterly anomalies from the idealized IOD forcing. A key feature of the third idealized experiment is the significant enhancement of easterly wind stress forcing to the south of the equator, which arises from the nonlinear dependence of wind stress on wind speed through the bulk formulas. Figure 10 shows plots of zonal wind stress anomalies for the three idealized experiments. Strong easterly wind stress anomalies can be seen to the south of the equator in Fig. 10c with maximum around 5°–7°S. It is important to recognize that the easterly wind stress anomalies in the third experiment (Fig. 10c) are much stronger than the sum of wind stress anomalies of the other two experiments (Figs. 10a,b). Even though the wind anomalies in Fig. 9c correspond to a linear superposition of the wind anomalies of Figs. 9a,b, the nonlinearity of the wind stress dependence on wind speed results in a nonlinear amplification of the wind stress, as evidenced from the strong easterly wind stress anomalies to the south of the equator (Fig. 10c).

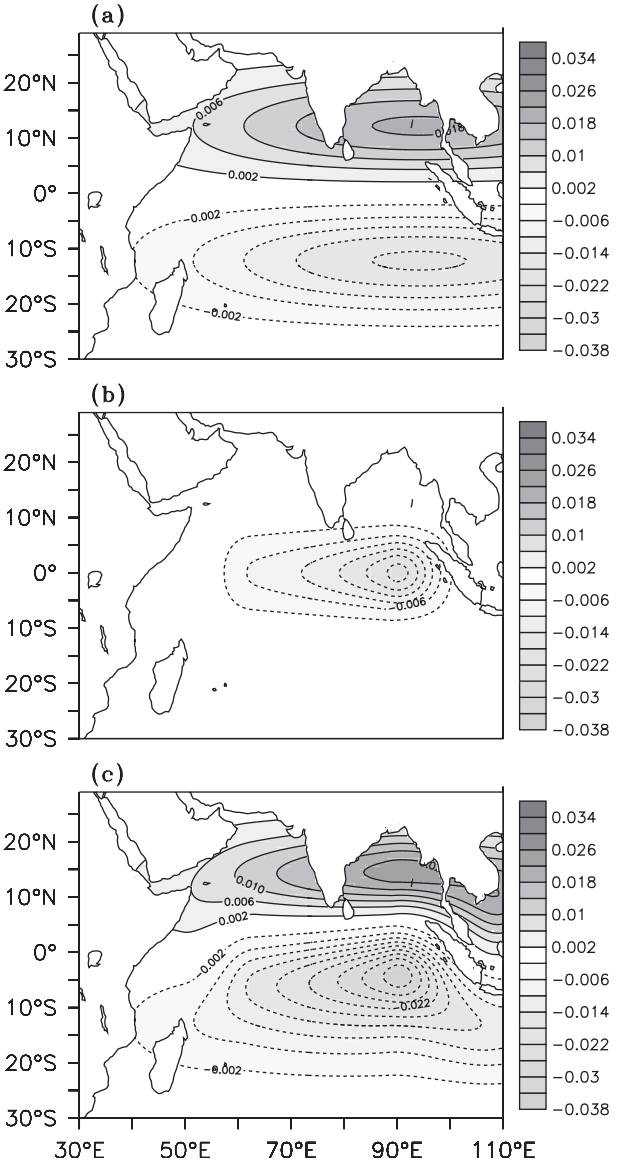

FIG. 10. Zonal component of wind stress (N m^{-2}) anomaly in the idealized forcing experiments: (a) Gill-type monsoonal wind forcing, (b) idealized IOD forcing, and (c) Gill-type monsoon + idealized IOD wind forcing.

d. Model-simulated response to idealized forcing

Longitude–depth sections of simulated temperature anomalies together with maps of d20 and current anomalies from the three idealized experiments are shown in Fig. 11. The temperature anomalies are averaged between the equator and 10°S. The response to the Gill-type monsoonal forcing is weak, with very slight cooling in the eastern IO and weak warm anomalies in the west (Figs. 11a,d). The temperature response in the idealized IOD simulation shows an enhanced east–west contrast with cold subsurface anomalies (~−3°C) in the eastern IO and warm anomalies (~1.5°C) in the western IO (Figs. 11b,e). This zonally asymmetric temperature response is significantly amplified in the combined (monsoon + IOD) forcing experiment (Figs. 11c,f), which shows strong subsurface cooling (~−4°C) in the eastern IO and anomalous warming (>+2.0°C) in the WIO. It is important to recognize that the temperature response in the combined (monsoon + IOD) experiment is stronger than the sum of the individual responses of the Gill-type monsoon and idealized IOD experiments, thus indicating the nonlinear character of the IO response to the

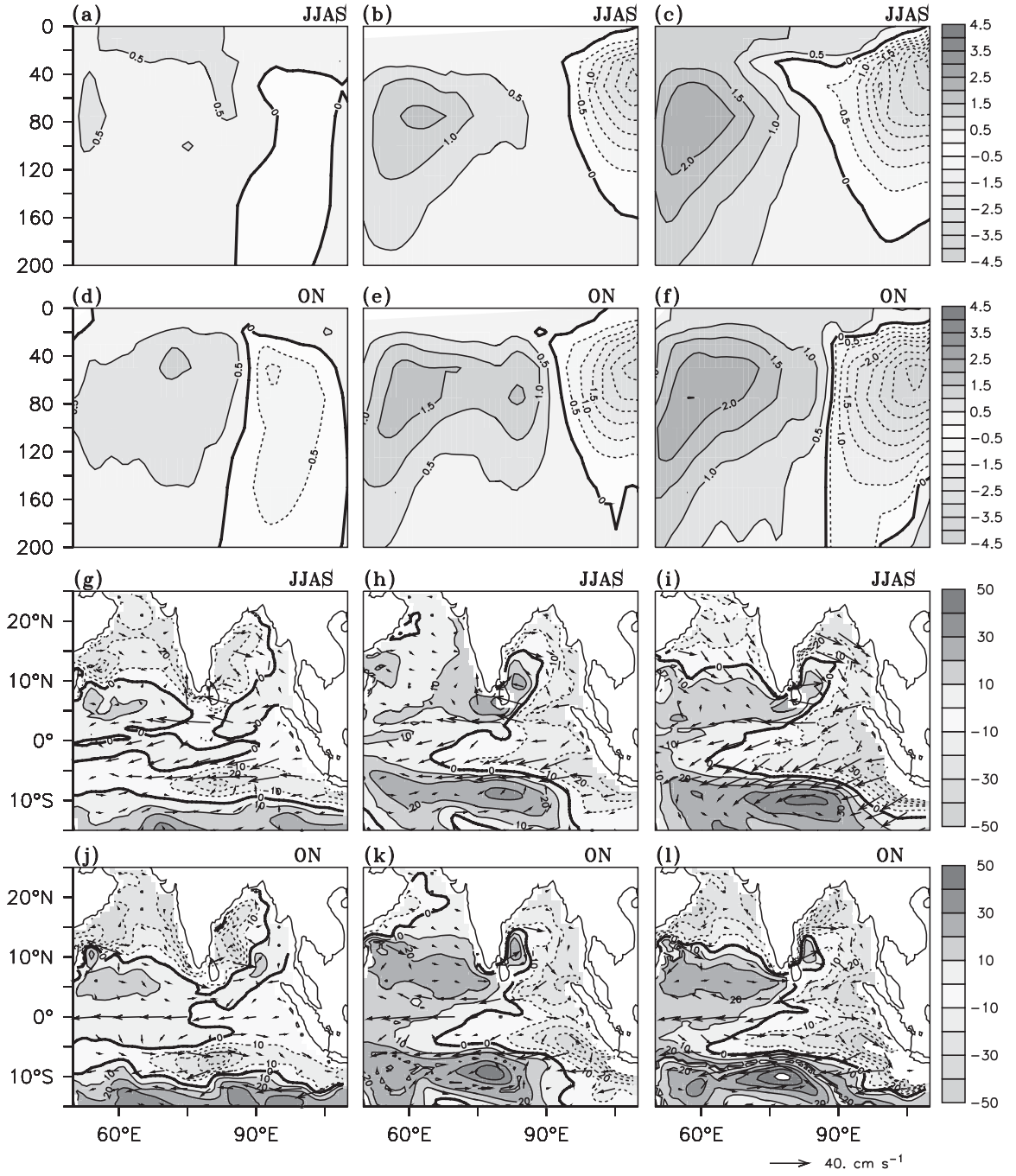

FIG. 11. (a)–(f) Longitude–depth sections of the simulated (°C) anomalies from the three idealized experiments. The temperature anomalies are averaged between equator and 10°S and shown for JJAS and ON seasons. (g)–(l) Anomalies of d20 (m) and currents (cm s^{-1}) simulated in the three idealized experiments. The first, second, and third columns correspond to the Gill-type monsoon, idealized IOD, and Gill-type monsoon + idealized IOD wind forcing experiments, respectively.

strong easterly wind stress associated with nonlinear amplification (see Fig. 10c).

The d20 and current response for the three idealized experiments are shown in Figs. 11g–l. The idealized IOD and the combined (monsoon + IOD) simulations show thermocline shoaling in the SETIO and deepening in the WIO, together with westward current anomalies. Also the zonal contrast of the d20 response is strongest in the combined (monsoon + IOD) simulation as compared to the other two cases. We computed the zonal difference

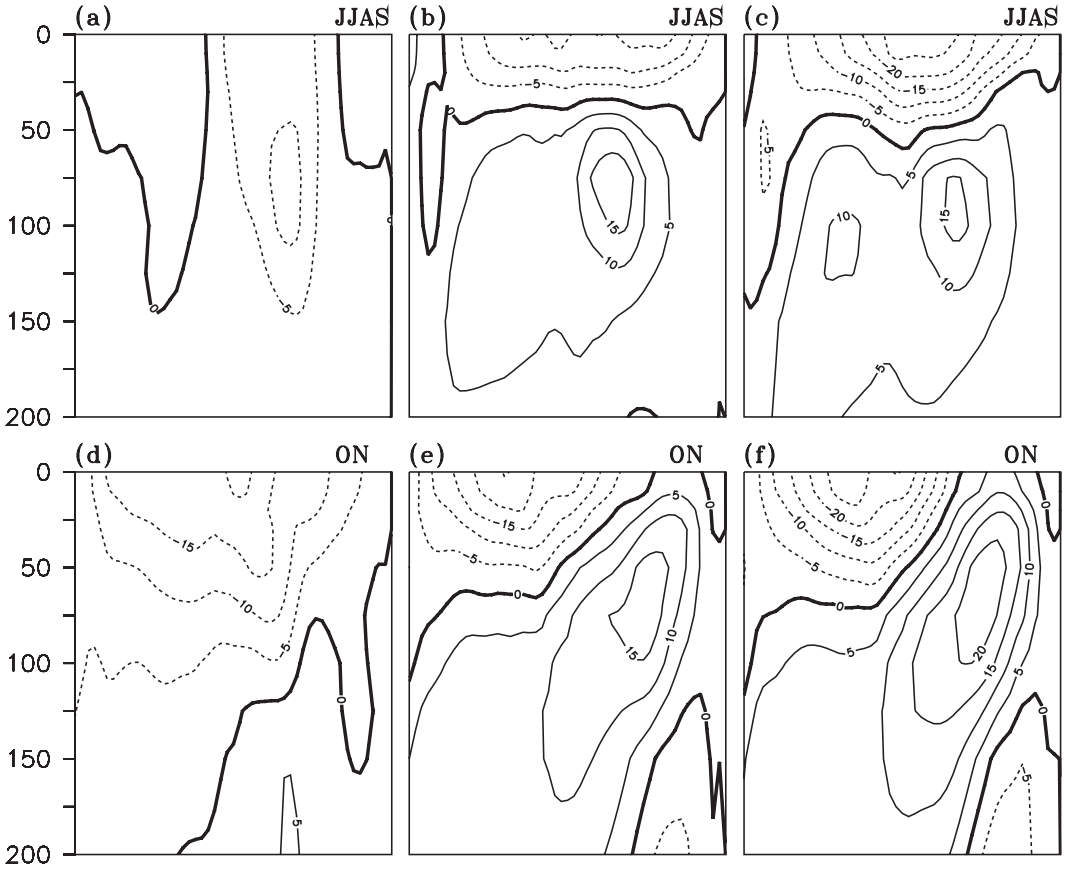

FIG. 12. (a)–(f) Longitude–depth sections of zonal current (cm s^{-1}) anomalies averaged between 2°S and 2°N from the three idealized experiments. The first, second, and third columns correspond to the Gill-type monsoon, idealized IOD, and Gill-type monsoon + idealized IOD wind forcing experiments, respectively.

(east minus west) in heat content anomalies in the upper 200 m between the eastern (10°S–equator, 85°–105°E) and western (10°S–equator, 45°–75°E) IO for the three idealized experiments. The zonal difference in the heat content anomaly was found to be -1.6×10^9 J m^{-2} in the combined (monsoon + IOD) experiment, which exceeds the sum of the zonal gradient of heat content anomalies from the idealized IOD (-1.1×10^9 J m^{-2}) and the Gill-type monsoon (-0.2×10^9 J m^{-2}) experiments. This suggests that the nonlinear amplification of the easterly wind stress anomalies to the south of the equator in the combined (monsoon + IOD) experiment can significantly amplify the zonal contrast of the IO heat content response as compared to the idealized IOD experiment.

Longitude–depth sections of zonal current anomalies from the three idealized experiments are shown in Fig. 12 for JJAS and ON seasons. The response in the Gill-type monsoon experiment is dominated by anomalous westward currents extending as deep as 150 m below the surface (Figs. 12a,b). However, the other two simulations [i.e., idealized IOD and the combined (monsoon + IOD) experiments] show anomalous westward currents in the upper 50–70 m and strong EUC anomalies at depths near 100 m (Figs. 12c–f). Notice that the EUC anomalies are more intensified in the combined (monsoon + IOD) simulation as compared to the idealized IOD case. As discussed earlier (Fig. 8), we have confirmed that the eastward EUC anomalies in the idealized IOD and monsoon + IOD simulations are associated with zonal pressure gradients in the subsurface along the equator arising because of pressure drop near 90°E (figures not shown).

Two points emerge from the above discussion. First, the patch of anomalous easterlies over the near-equatorial region is effective in producing the EUC as noted by previous studies in the Indian, Atlantic, and Pacific Oceans (e.g., Philander and Pacanowski 1980; McCreary 1981, 1985; McPhaden 1993; Izumo 2005; Reppin et al. 1999). The second point is that the superposition of the monsoon-type off-equatorial wind anomaly on the off-equatorial easterly anomalies leads to nonlinear intensification of the easterly wind stress anomalies to the south of the

equator. The issue that warrants an explanation is the physical mechanism through which the intensified off-equatorial easterly wind stress anomalies can modify the EUC. Pedlosky (1987) proposed a simple model of the EUC that is dynamically linked with the geostrophic regime of the subtropical gyre and involves a shallow meridional overturning circulation that feeds the eastward-accelerating EUC. In the present context, it would be relevant to understand whether the intensification of the AH over the southern subtropics during positive IOD events and the amplification of the easterly wind stress anomalies to the south of the equator can strengthen the shallow meridional overturning circulation. Such a mechanism would enhance the feed into the EUC and can produce strong cooling in the east. We will discuss this issue in section 5f.

e. Understanding the heat content response during IOD-SMON and IOD-WMON

Maps of upper-ocean heat content and SST anomalies for the IOD-SMON and IOD-WMON cases are shown in Fig. 13. It can be seen that the east–west gradient of the IO heat content and SST anomalies are clearly enhanced in IOD-SMON (Figs. 13a,b) as compared to IOD-WMON (Figs. 13c,d). This suggests that, if the monsoon flow strengthens during a positive IOD, then it can act to further amplify the zonal contrast of the IO anomalies. In other words, the findings raise the possibility of a positive feedback between the monsoon and IOD, which can reinforce the zonal contrast of the IO heat content and SST anomalies. In this feedback, a positive IOD would favor an intensified summer monsoon circulation and increased precipitation over the Indian landmass, so that the strong ascending motions over the subcontinent would cause subsidence over the SH subtropics through the reverse monsoon Hadley cell, leading to an intensification of the AH and strengthening of the off-equatorial easterly anomalies that extend out to nearly 20°S, and might be also described in terms of the Matsuno–Gill pattern (Matsuno 1966; Gill 1980; see Fig. 9a). This feature can be seen in coupled model simulations (e.g., Lau and Nath 2004; see their Figs. 8a–c). In turn, the strong monsoon off-equatorial easterly anomalies would favor increased upwelling and cooling in the SETIO along Sumatra, thereby giving rise to enhanced zonal contrast of the IO heat content anomalies. In other words, a dipolelike response, once triggered by a patch of equatorial easterlies, can be further amplified by the off-equatorial easterlies associated with the enhanced boreal summer monsoon circulation. The mechanism seems to work also with opposite signs. It is noted that negative IODs co-occurring with weak monsoons had stronger zonal contrast (i.e., anomalous warming in east and cooling in west) than those accompanying strong monsoons (fig not shown).

Two additional idealized experiments are carried out to understand how contrasting summer monsoon flow patterns can alter the IO response during IOD events. The first experiment uses a wind forcing (Fig. 14a) that is a combination of a Gill-type strong monsoon anomaly and an idealized IOD wind forcing (i.e., same as Fig. 9c). In the second experiment, the wind forcing is a combination of a Gill-type weak monsoon wind anomaly and an idealized IOD wind forcing (Fig. 14b). The zonal and meridional components of the Gill-type weak monsoon anomaly are taken to be opposite to those of the strong monsoon case, while the idealized IOD wind forcing is identical in the two experiments (same as Fig. 14b). The simulated heat content and SST response in the two experiments is shown in Figs. 14c–f. The heat content and SST anomalies are consistent in showing an increased zonal contrast in the strong monsoon + IOD idealized simulation as compared to the weak monsoon + IOD case. The differences in the SST response in the western Arabian Sea between Fig. 14e and Fig. 14f reflect the ocean response typically observed during strong and weak monsoons (Babu and Joseph 2002; Ramesh and Krishnan 2005). Despite the presence of equatorial easterlies, it is interesting to note weaker zonal contrast of the heat content and SST anomalies in the latter simulation in response to the weakened monsoon off-equatorial wind anomalies to the south of the equator. Furthermore, the influence of strong and weak monsoon wind forcing on the heat content and SST response can be discerned during the ON months when IOD events attain their mature phase (see Fig. 15).

f. Physical mechanism linking the off-equatorial winds and the EUC during IOD events

It is known from earlier studies that the EUCs in the Pacific and Atlantic Oceans are fed by shallow meridional circulation cells extending from the subtropics to the equator (e.g., Pedlosky 1987; McCreary and Lu 1994; Izumo 2005). In the tropics, the subsurface branch of this cell contributes to the transport of EUC and then upwells into the surface layers in the eastern equatorial ocean and flows poleward out of the tropics. In the subtropics, surface water subducts into the thermocline and flows equatorward in the subtropical gyre; part of it eventually moves into the equatorial ocean to close the cell. In the IO, the meridional overturning circulation is a shallow ($z \geq -500$ m) cross-equatorial circulation consisting of northward flow of SH thermocline water; upwelling in the NH off Somalia, Oman, and India; and a return flow of surface water (see Schott and McCreary 2001; Schott et al. 2002; Miyama et al. 2003). There are

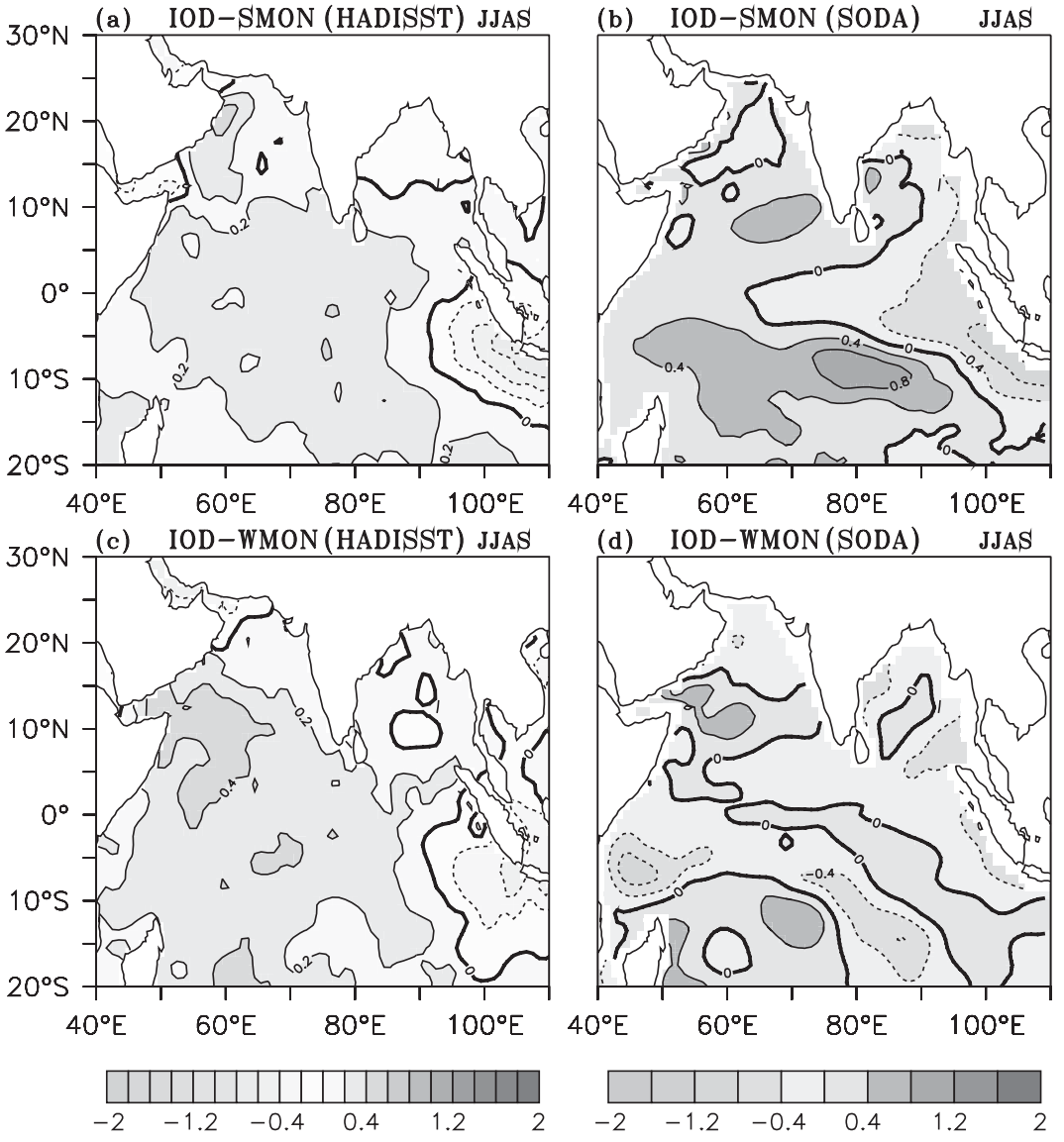

FIG. 13. Composite maps of (left) SST (°C) anomalies and (right) heat content ($\times 10^9$ J m^{-2}) anomalies in the upper 300 m for the (a),(b) IOD-SMON and (c),(d) IOD-WMON cases. The SST data are based on HadISST1.1 and the heat content is from SODA.

two other shallow overturning circulations that are defined by upwelling regions in the SH. One is closed by upwelling around 5°–10°S in the central and western ocean and has been described in several studies (Murtugudde et al. 1999; Schott and McCreary 2001; Schott et al. 2002; Xie et al. 2002; Yokoi et al. 2009; Hermes and Reason 2008). The other circulation is associated with upwelling in the eastern equatorial ocean along the Java and Sumatran coasts and occasionally along the equator (see Miyama et al. 2003; Schott et al. 2002).

Here, we examine the possible role of the off-equatorial monsoon easterly anomalies in affecting the upwelling in the equatorial eastern IO via changes in the transient shallow meridional circulation during IOD events. We follow the approach of Izumo (2005) to illustrate the shallow meridional circulation anomalies using the zonal, meridional, and vertical currents. Figures 16a,b are latitude–depth sections depicting the anomalous shallow meridional overturning circulations and zonal current anomalies for the IOD-SMON and IOD-WMON cases based on SODA. The current anomalies are averaged zonally between 90° and 100°E in the eastern IO. In the IOD-SMON case (Fig. 16a), equatorial upwelling and anomalous southward near-surface flow can be noticed diverging away from the equator. The subsurface zonal current anomalies in the equatorial region in Fig. 16a

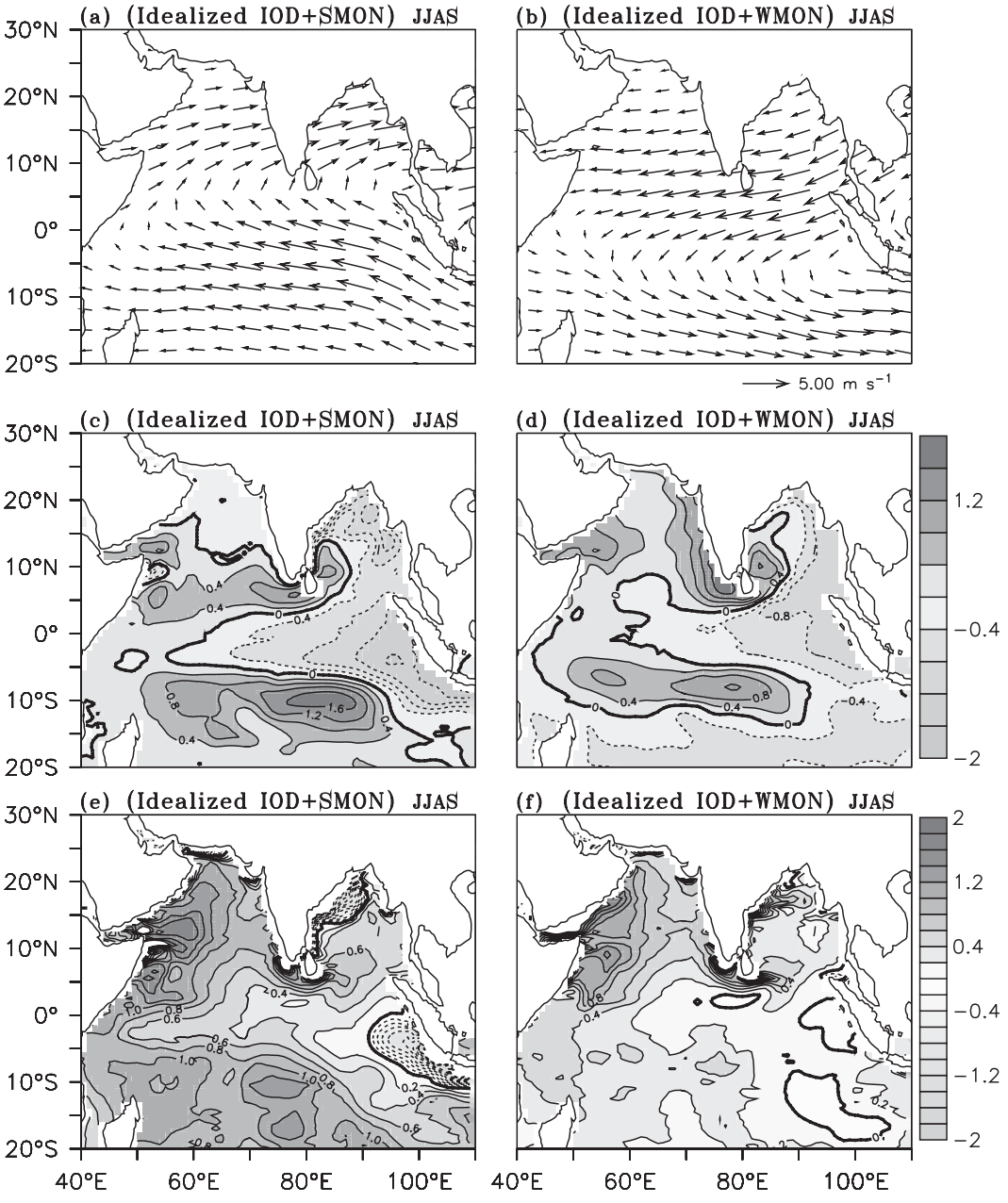

FIG. 14. (a),(b) Anomaly maps of idealized wind forcing (m s^{-1}); (c),(d) OGCM simulated heat content ($\times 10^9$ J m^{-2}); and (e),(f) SST (°C) response in the two idealized experiments for JJAS months. (left) The idealized IOD + Gill-type strong monsoon case; (right) the idealized IOD + Gill-type weak monsoon case.

show positive values corresponding to the enhanced EUC. However, in the IOD-WMON case, the EUC anomalies are practically absent (Fig. 16b).

The overall features of the meridional circulation anomalies discussed above are also brought out in the two idealized model simulations, that is, IOD + strong monsoon and IOD + weak monsoon (see Figs. 16c,d). The vector field in Fig. 16c shows equatorial upwelling, anomalous southward near-surface flow, and downwelling to the south. The near-surface southward current anomalies in Fig. 16c, which extend from the NH across the equator to the SH, resemble the idealized response obtained by Miyama et al. (2003) to an antisymmetric wind forcing w.r.t. the equator (see their Fig. 10, bottom-right panel). The subsurface anomalies in Fig. 16c show anomalous northward currents below 50 m extending from about 12°S up to the equator. An additional important feature in Fig. 16c is the enhanced EUC

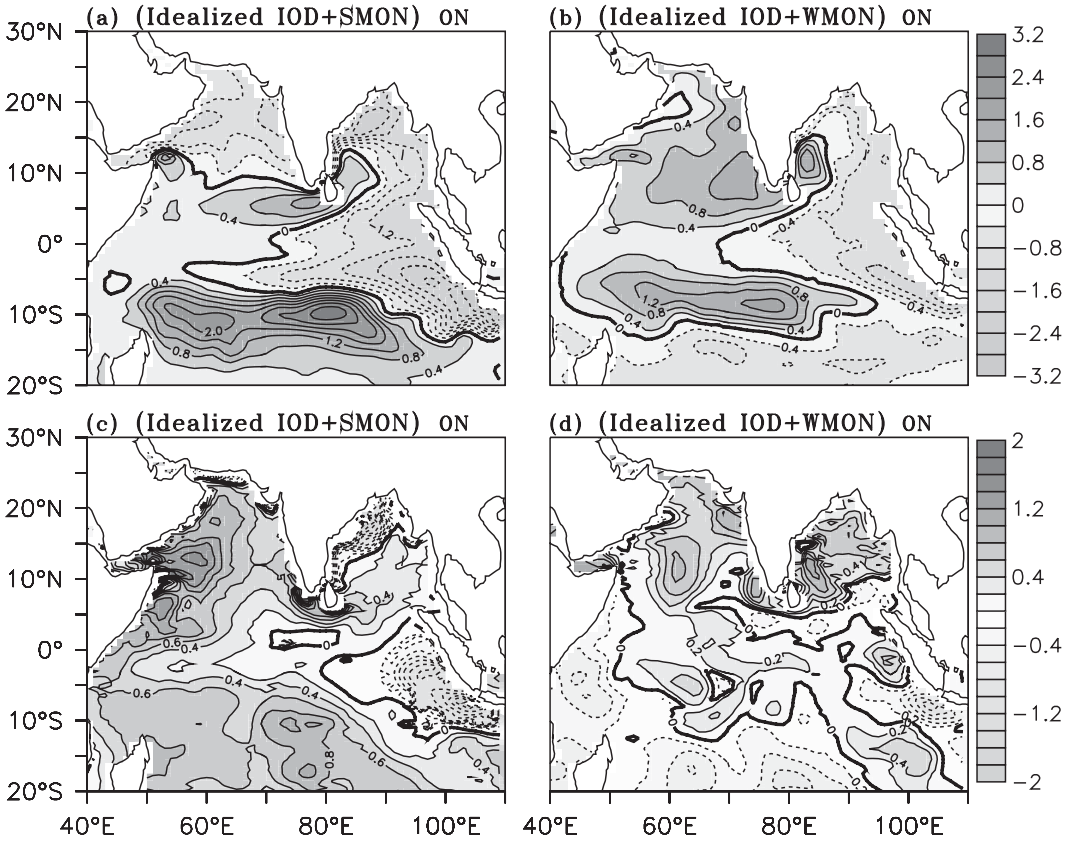

FIG. 15. (a),(b) Anomalies of the OGCM simulated heat content ($\times 10^9$ J m^{-2}) and (c),(d) SST (°C) response in the two idealized experiments for ON. (left) The idealized IOD + Gill-type strong monsoon case; (right) the idealized IOD + Gill-type weak monsoon case.

anomalies that are accompanied by equatorial upwelling. Basically, the off-equatorial easterly winds create poleward Ekman surface transport to the south, and hence downwelling to the south, and equatorial divergence that causes equatorial upwelling. These processes together can be interpreted as an increase of the tropical meridional overturning circulation that will actually feed the southern part of the EUC (see Blanke and Raynaud 1997; Masson et al. 2004). It is interesting to note that the model response in the idealized (IOD + weak monsoon) experiment (Fig. 16d) does not capture the eastward EUC anomalies and the shallow meridional circulation anomalies. In short, the results presented in Figs. 16a,c raise the possibility that an intensification of the AH and anticyclonic circulation over the SH can strengthen the transient shallow meridional overturning circulation in the eastern IO and thereby enhance the feed of cold subsurface off-equatorial waters to the EUC and the upwelling off Java–Sumatra. Thus the transient shallow meridional overturning circulations can mediate the dynamical link between the transient EUCs and the off-equatorial circulation anomalies. Also, the above physical mechanism provides a plausible explanation through which the off-equatorial intensification of the monsoon easterly winds can influence the IO response during IOD events. A concise synthesis of the main physical mechanisms through which the summer monsoon flow can influence the IOD is schematically illustrated in Fig. 17.

6. Summary and conclusions

Studies have shown that positive IOD events generally tend to favor increased summer monsoon precipitation over the Indian landmass through enhanced cross-equatorial transport of moisture into the subcontinent. In fact, a majority of positive IOD events in the last 50 years were associated with above-normal summer monsoon precipitation over central-north India and intensified monsoon circulation. Since the IOD phenomenon evolves through the boreal summer season and attains peak amplitude in autumn, a question arises as to whether the strengthening of the summer monsoon flow can shape the IOD evolution. To address this question,

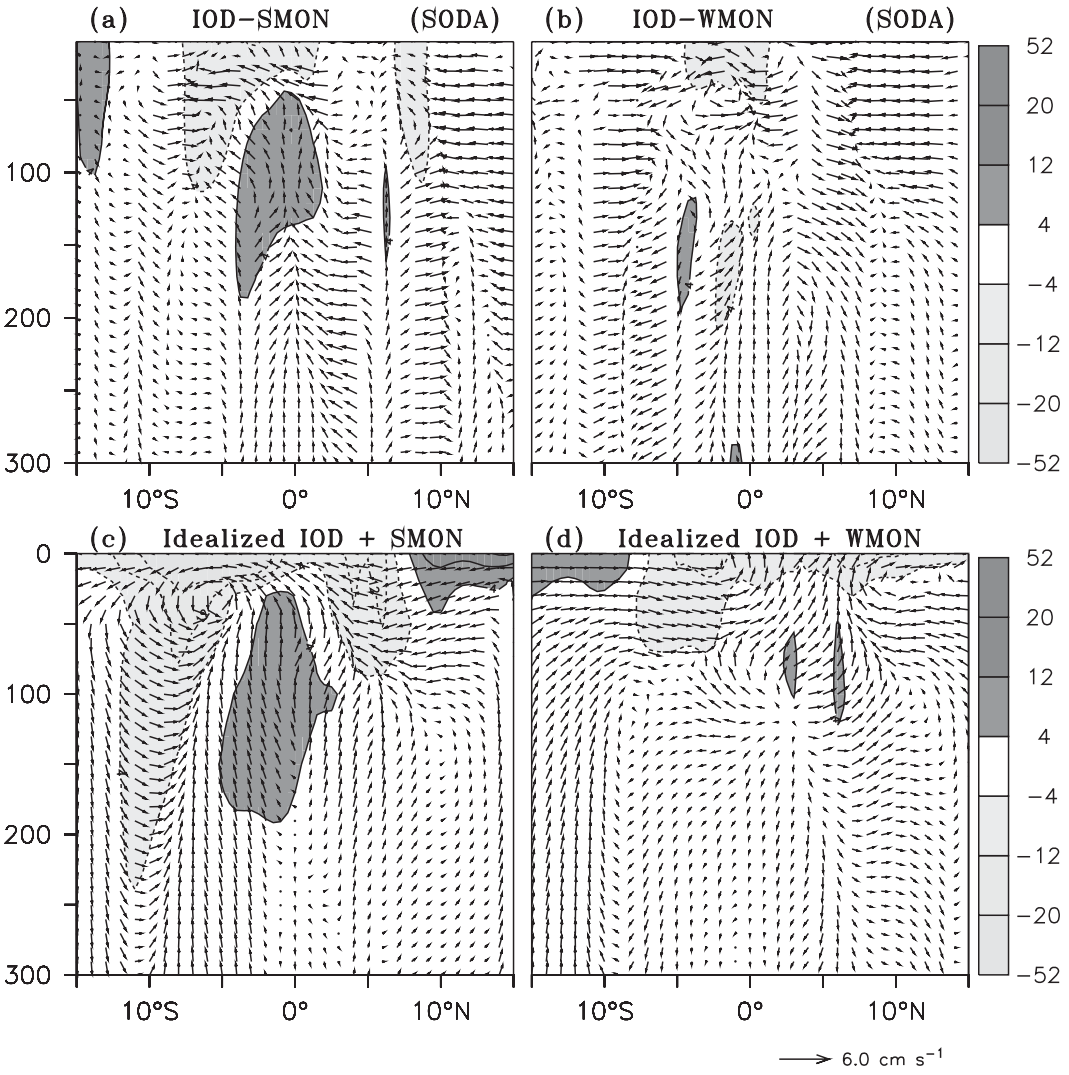

FIG. 16. Latitude–depth sections of zonal current (cm s^{-1}) anomalies (shading) and shallow meridional overturning circulation anomalies (vector). The zonal, meridional, and vertical velocities are zonally averaged between 90° and 100°E. (a),(b) The anomalies are based on SODA; (c),(d) the anomalies are from the idealized model runs. (a) IOD-SMON, (b) IOD-WMON, (c) idealized IOD + strong monsoon, and (d) idealized IOD + weak monsoon.

we have conducted a series of numerical simulation experiments using a regional IO model along with supplementary data diagnostics. The model experiments and analysis were focused on two sets of positive IOD events—namely, IOD-SMON and IOD-WMON—that co-occurred with periods of above-normal and below-normal Indian summer monsoons. In addition to the observed IOD cases, further model experiments were conducted using idealized wind forcing. The results from the model simulations and the data diagnostic analysis allow us to interpret and substantiate the monsoonal flow effects on the IO dynamics during IOD events.

The findings suggest that, if the summer monsoon flow strengthens during a positive IOD, it can act to further amplify the zonal contrast of the IO heat content anomalies. The comprehensive physical processes through which the monsoonal winds can influence the IOD are schematically portrayed in Fig. 17. Basically the enhanced monsoon precipitation over the Indian landmass during IOD-SMON and the associated strengthening of the monsoon reverse Hadley circulation would induce strong easterlies to the south of the equator and thereby encourage stronger upwelling and cooling in the SETIO. It is noted that an intensified summer monsoon flow together with easterly anomalies over the equatorial IO can significantly reinforce the east-to-west contrast of the upper-ocean heat content anomalies as compared to a wind forcing having only easterly anomalies over the

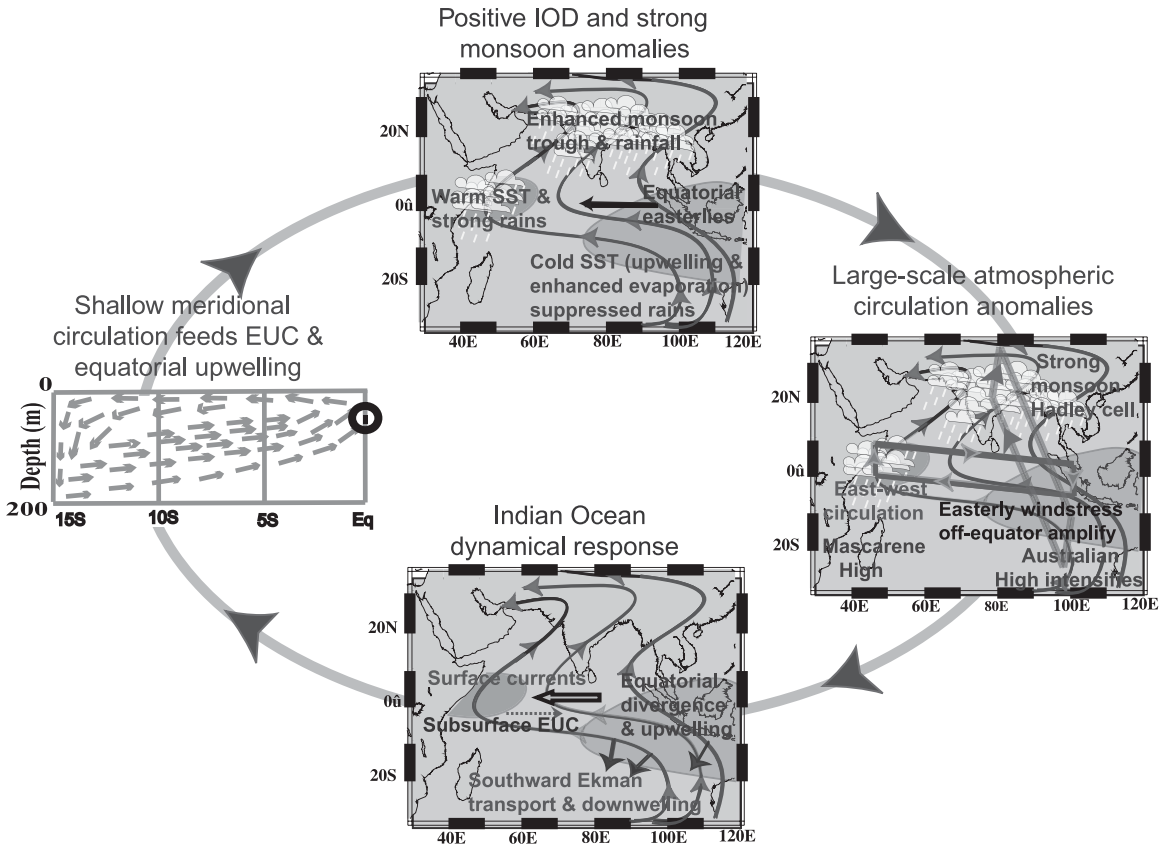

FIG. 17. Schematic of the feedback of a stronger-than-normal summer monsoon flow on the Indian Ocean response during positive IOD events.

equatorial IO. Because of the nonlinear dependence of wind stress on wind speed, the combined effect of superposing the easterly wind anomalies of the IOD and the monsoon off-equatorial southeasterly anomalies produces a nonlinear amplification of the easterly wind stress anomalies to the south of the equator. As the strong easterlies force upwelling in the eastern equatorial IO, the thermocline shoaling in the east provides a zonal pressure gradient along the equator that drives transient eastward EUCs that deliver cold subsurface water to the equatorial and Sumatra upwelling. Furthermore, the findings indicate that the strengthening of the AH during IOD-SMON periods favors intensification of transient shallow meridional overturning circulations, which enhance the feed of cold subsurface off-equatorial waters to the southern part of the EUC. This feature is associated with anomalous southward Ekman surface transport and downwelling to the south between 5° and 15°S, equatorward flow in the subsurface, and upwelling in the equatorial eastern IO off Java–Sumatra. Thus the shallow meridional overturning circulation in the eastern IO provides a dynamical link between the off-equatorial circulation anomalies and the transient EUCs and offers a physical mechanism through which an off-equatorial intensification of monsoon easterly winds can influence the IO response during IOD events. In bringing out the effect of the summer monsoon flow on the zonal gradient of the IO heat content response, the present findings raise the possibility of an interactive feedback between the monsoon and IOD that can actually affect the strength of the IOD. The proposed feedback could be tested by coupled model experiments. The use of a stand-alone OGCM has been a caveat in terms of quantifying the coupled interactions. Further studies using fully coupled climate models will be needed to unravel the details of the interactive feedbacks.

Acknowledgments. We are grateful to Professors Jay McCreary, Julia Slingo, and B. N. Goswami for all their suggestions. The author PS thanks Dr. N. A. Diansky, Institute of Numerical Mathematics, Russia, for providing the OGCM. We thank the Editor, Dr. Shang Ping Xie, the anonymous reviewers, and the Associate Editor for their constructive comments. The work was supported under the DOD/INDOMOD-SATCORE (ISP 1.5) project, Government of India.

REFERENCES

Alekseev, V. V., and V. B. Zalesny, 1993: Numerical model of large scale dynamics of ocean (in Russian). *Numerical Processes and Systems,* G. I. Marchuk, Ed., Nayka, Vol. 10, 232–252.

Alexander, M. A., I. Blade, M. Newman, J. R. Lazante, N.-C. Lau, and J. D. Scott, 2002: The atmospheric bridge: The influence of ENSO teleconnections on air–sea interaction over global oceans. *J. Climate,* **15,** 2205–2231.

Annamalai, H., and R. Murtugudde, 2004: Role of the Indian Ocean in regional climate variability. *Earth's Climate: The Ocean–Atmosphere Interaction, Geophys. Monogr.,* Vol. 147, Amer. Geophys. Union, 213–246.

——, ——, J. Potemra, S. P. Xie, P. Liu, and B. Wang, 2003: Coupled dynamics over the Indian Ocean: Spring initiation of the zonal mode. *Deep-Sea Res.,* **50,** 2305–2330.

Ashok, K., Z. Guan, and T. Yamagata, 2001: Impact of the Indian Ocean dipole on the relationship between the Indian monsoon rainfall and ENSO. *Geophys. Res. Lett.,* **28,** 4499–4502.

——, ——, N. H. Saji, and T. Yamagata, 2004: On the individual and combined influence of the ENSO and the Indian Ocean dipole on the Indian summer monsoon. *J. Climate,* **17,** 3141–3154.

Babu, C. A., and P. V. Joseph, 2002: Post-monsoon sea surface temperature and convection anomalies over Indian and Pacific Oceans. *Int. J. Climatol.,* **22,** 559–567, doi:10.1002/joc.729.

Behera, S. K., R. Krishnan, and T. Yamagata, 1999: Unusual ocean-atmosphere conditions in the tropical Indian Ocean during 1994. *Geophys. Res. Lett.,* **26,** 3001–3004.

Bender, C. M., and S. A. Orszag, 1978: *Advanced Mathematical Methods for Scientists and Engineers*. McGraw-Hill, 593 pp.

Black, E., J. M. Slingo, and K. R. Sperber, 2003: An observational study of the relationship between excessively strong short rains in coastal East Africa and Indian Ocean SST. *Mon. Wea. Rev.,* **131,** 74–94.

Blanke, B., and S. Raynaud, 1997: Kinematics of the Pacific Equatorial Undercurrent: An Eulerian and Lagrangian approach from GCM results. *J. Phys. Oceanogr.,* **27,** 1038–1053.

Carton, J. A., G. Chepurin, X. Cao, and B. Giese, 2000: A simple ocean data assimilation analysis of the upper ocean 1950–95. Part I: Methodology. *J. Phys. Oceanogr.,* **30,** 294–309.

Cherchi, A., S. Gualdi, S. Behera, J. J. Luo, S. Masson, T. Yamagata, and A. Navarra, 2007: The influence of tropical Indian Ocean SST on the Indian summer monsoon. *J. Climate,* **20,** 3083–3105.

de Boyer Montégut, C., G. Madec, A. S. Fischer, A. Lazar, and D. Iudicone, 2004: Mixed layer depth over the global ocean: An examination of profile data and profile-based climatology. *J. Geophys. Res.,* **109,** C12003, doi:10.1029/2004JC002378.

Diansky, N. A., A. V. Bagno, and V. B. Zalesny, 2002: Sigma model of global ocean circulation and its sensitivity to variations in wind stress. *Izv. Atmos. Ocean. Phys.,* **38,** 537–556.

——, V. B. Zalesny, S. N. Moshonkin, and A. S. Rusakov, 2006: High resolution modeling of the monsoon circulation in the Indian Ocean. *Oceanology (Moscow),* **46,** 608–628.

Drbohlav, H.-K. L., G. Gualdi, and A. Navarra, 2007: A diagnostic study of the Indian Ocean dipole mode in El Niño and non–El Niño years. *J. Climate,* **20,** 2961–2977.

Feng, M., and G. Meyers, 2003: Interannual variability in the tropical Indian Ocean: A two-year time scale of IOD. *Deep-Sea Res.,* **50,** 2263–2284.

——, ——, and S. Wijffels, 2001: Interannual upper ocean variability in the tropical Indian Ocean. *Geophys. Res. Lett.,* **28,** 4151–4154.

Gadgil, S., P. N. Vinayachandran, P. A. Francis, and S. Gadgil, 2004: Extremes of the Indian summer monsoon rainfall, ENSO and equatorial Indian Ocean oscillation. *Geophys. Res. Lett.,* **31,** L12213, doi:10.1029/2004GL019733.

Gill, A. E., 1980: Some simple solutions for heat induced tropical solutions. *Quart. J. Roy. Meteor. Soc.,* **106,** 447–462.

Gualdi, S., E. Guilyardi, A. Navarra, S. Masina, and P. Delecluse, 2003: The interannual variability in the tropical Indian Ocean as simulated by a CGCM. *Climate Dyn.,* **20,** 567–582.

Hermes, J., and C. J. C. Reason, 2008: Annual cycle of the South Indian Ocean (Seychelles-Chagos) thermocline ridge in a regional ocean model. *J. Geophys. Res.,* **113,** C04035, doi:10.1029/2007JC004363.

Izumo, T., 2005: The equatorial undercurrent, meridional overturning circulation and their roles in mass and heat exchanges during El Niño events in the tropical Pacific Ocean. *Ocean Dyn.,* **55,** 110–123.

——, C. de Boyer Montégut, J.-J. Luo, S. K. Behera, S. Masson, and T. Yamagata, 2008: The role of the western Arabian Sea upwelling in Indian monsoon rainfall variability. *J. Climate,* **21,** 5603–5623.

Kistler, R., and Coauthors, 2001: The NCEP–NCAR 50-Year Reanalysis: Monthly means CD-ROM and documentation. *Bull. Amer. Meteor. Soc.,* **82,** 247–267.

Kripalani, R. H., J. H. Oh, J. H. Kang, S. S. Sabade, and A. Kulkarni, 2005: Extreme monsoons over East Asia: Possible role of Indian Ocean zonal mode. *Theor. Appl. Climatol.,* **82,** 81–94.

Krishnan, R., 1993: Dynamics of large-scale heat induced circulations in the tropical atmosphere. Ph.D. thesis, University of Pune, 154 pp.

Lakshmi, A. S. N., V. S. N. Murty, R. Murtugudde, M. Anil Kumar, M. S. S. Sarma, Y. Agarvadekar, and A. Almeida, 2007: Semiannual variability in the observed and OGCM simulated zonal currents in the equatorial Indian Ocean. *Proc. Celebrating the Monsoon: An Int. Monsoon Conf.,* Bangalore, India, Indian Institute of Science, 11 pp.

Lau, N.-C., and M. J. Nath, 2000: Impact of ENSO on the variability of the Asian-Australian monsoons as simulated in GCM experiments. *J. Climate,* **13,** 4287–4309.

——, and ——, 2004: Coupled GCM simulation of atmosphere–ocean variability associated with zonally asymmetric SST changes in the tropical Indian Ocean. *J. Climate,* **17,** 245–265.

Lu, P., J. P. McCreary, and B. A. Klinger, 1998: Meridional circulation cells and the source waters of the Pacific Equatorial Undercurrent. *J. Phys. Oceanogr.,* **28,** 62–64.

Masson, S., J.-P. Boulanger, C. Menkes, P. Delecluse, and T. Yamagata, 2004: Impact of salinity on the 1997 Indian Ocean dipole event in a numerical experiment. *J. Geophys. Res.,* **109,** C02002, doi:10.1029/2003JC001807.

Masumoto, Y., H. Hase, Y. Kuroda, H. Matsuura, and K. Takeuchi, 2005: Intraseasonal variability in the upper layer currents observed in the eastern equatorial Indian Ocean. *Geophys. Res. Lett.,* **32,** L02607, doi:10.1029/2004GL021896.

Matsuno, T., 1966: Quasi-geostrophic motions in the equatorial area. *J. Meteor. Soc. Japan,* **44,** 25–42.

McCreary, J. P., 1981: A linear stratified model of the equatorial undercurrent. *Philos. Trans. Roy. Soc. London,* **A298,** 603–635.

——, 1985: Modeling equatorial ocean circulation. *Annu. Rev. Fluid Mech.,* **17,** 359–409.

——, and P. Lu, 1994: Interaction between the subtropical and equatorial ocean circulations: The subtropical cell. *J. Phys. Oceanogr.,* **24,** 466–497.

McPhaden, M. J., 1993: Trade wind fetch related variations in equatorial undercurrent depth, speed and transport. *J. Geophys. Res.,* **98,** 2555–2559.

Meyers, G., P. McIntosh, L. Pigot, and M. Pook, 2007: The years of El Niño, La Niña, and interactions with the tropical Indian Ocean. *J. Climate,* **20,** 2872–2880.

Miyama, T., J. P. McCreary, T. G. Jensen, J. Loschnigg, S. Godfrey, and A. Ishida, 2003: Structure and dynamics of the Indian Ocean cross-equatorial cell. *Deep-Sea Res. II,* **50,** 2023–2047.

Molinari, R. L., D. Olson, and G. Reverdin, 1990: Surface current distributions in the tropical Indian Ocean derived from compilations of surface buoy trajectories. *J. Geophys. Res.,* **95,** 7217–7238.

Murtugudde, R., S. Signorini, J. Christian, A. Busalacchi, and C. McClain, 1999: Ocean color variability of the tropical Indo-Pacific basin observed by SeaWiFS during 1997–98. *J. Geophys. Res.,* **104,** 18 351–18 366.

——, J. P. McCreary, and A. J. Busalacchi, 2000: Oceanic processes associated with anomalous events in the Indian Ocean with relevance to 1997–1998. *J. Geophys. Res.,* **105,** 3295–3306.

Pacanowski, R. C., and S. G. H. Philander, 1981: Parameterization of vertical mixing in numerical models of the tropical ocean. *J. Phys. Oceanogr.,* **11,** 1442–1451.

Pedlosky, J., 1987: An inertial theory of the equatorial undercurrent. *J. Phys. Oceanogr.,* **17,** 1978–1985.

Philander, S. G. H., and R. Pacanowski, 1980: The generation of equatorial currents. *J. Geophys. Res.,* **85,** 1123–1136.

Rajeevan, M., J. Bhate, J. D. Kale, and B. Lal, 2006: A high-resolution daily gridded rainfall for the Indian region: Analysis of break and active monsoon spells. *Curr. Sci.,* **91,** 296–306.

Ramesh, K. V., and R. Krishnan, 2005: Coupling of mixed layer processes and thermocline variations in the Arabian Sea. *J. Geophys. Res.,* **110,** C05005, doi:10.1029/2004JC002515.

Rao, S. A., S. K. Behera, Y. Masumoto, and T. Yamagata, 2002: Interannual variability in the subsurface tropical Indian Ocean with a special emphasis on the Indian Ocean Dipole. *Deep-Sea Res.,* **49,** 1549–1572.

Rayner, N. A., D. E. Parker, E. B. Horton, C. K. Folland, L. V. Alexander, D. P. Rowell, E. C. Kent, and A. Kaplan, 2003: Global analyses of sea surface temperature, sea ice, and night marine air temperature since the late nineteenth century. *J. Geophys. Res.,* **108,** 4407, doi:10.1029/2002JD002670.

Reppin, J., F. A. Schott, J. Fischer, and D. Quadfasel, 1999: Equatorial currents and transports in the upper central Indian Ocean: Annual cycle and interannual variability. *J. Geophys. Res.,* **104,** 15 495–15 514.

Reverdin, G., D. Cadet, and D. Gutzler, 1986: Interannual displacements of convection and surface circulation over the equatorial Indian Ocean. *Quart. J. Roy. Meteor. Soc.,* **112,** 43–67.

Saji, N. H., B. N. Goswami, P. N. Vinayachandran, and T. Yamagata, 1999: A dipole mode in the tropical Indian Ocean. *Nature,* **401,** 360–363.

——, S.-P. Xie, and T. Yamagata, 2006: Tropical Indian Ocean variability in the IPCC twentieth-century climate simulations. *J. Climate,* **19,** 4397–4417.

Schott, F., 1983: Monsoon response of the Somali Current and associated upwelling. *Prog. Oceanogr.,* **12,** 357–382.

——, and J. P. McCreary, 2001: The monsoon circulation of the Indian Ocean. *Prog. Oceanogr.,* **51,** 1–123.

——, M. Dengler, and R. Schoenefeldt, 2002: Observations of shallow cross-equatorial cells in the Indian Ocean. *Prog. Oceanogr.,* **53,** 57–103.

Shukla, J., 1975: Effect of Arabian sea-surface temperature anomaly on Indian summer monsoon: A numerical experiment with the GFDL model. *J. Atmos. Sci.,* **32,** 503–511.

Slingo, J. M., and H. Annamalai, 2000: 1997: The El Niño of the century and the response of the Indian summer monsoon. *Mon. Wea. Rev.,* **128,** 1778–1797.

Stommel, H., 1960: Wind-drift near the equator. *Deep-Sea Res.,* **6,** 298–302.

Swapna, P., and R. Krishnan, 2008: Equatorial undercurrents associated with Indian Ocean Dipole events during contrasting summer monsoons. *Geophys. Res. Lett.,* **35,** L14S04, doi:10.1029/2008GL033430.

Tao, S., and L. Chen, 1987: A review of recent research on the East Asian summer monsoon in China. *Monsoon Meteorology,* C.-P. Chang and T. N. Krishnamurti, Eds., 60–92.

Terray, P., F. Chauvin, and H. Douville, 2007: Impact of southeast Indian Ocean sea surface temperature anomalies on monsoon–ENSO–dipole variability in a coupled ocean–atmosphere model. *Climate Dyn.,* **28,** 553–580.

Vecchi, G. A., and D. E. Harrison, 2004: Interannual Indian rainfall variability and Indian Ocean sea surface temperature anomalies. *Earth's Climate: The Ocean–Atmosphere Interaction, Geophys. Monogr.,* Vol. 147, Amer. Geophys. Union, 247–259.

Vinayachandran, P. N., N. H. Saji, and T. Yamagata, 1999: Response of the equatorial Indian Ocean to an anomalous wind event during 1994. *Geophys. Res. Lett.,* **26,** 1613–1616.

——, S. Iizuka, and T. Yamagata, 2002: Indian Ocean dipole mode events in an ocean general circulation model. *Deep-Sea Res.,* **49,** 1573–1596.

Wacongne, S., 1990: On the difference in strength between Atlantic and Pacific undercurrents. *J. Phys. Oceanogr.,* **20,** 792–799.

Webster, P. J., A. M. Moore, J. P. Loschnigg, and R. R. Leben, 1999: Coupled ocean–atmosphere dynamics in the Indian Ocean during 1997–98. *Nature,* **401,** 356–360.

Weller, R. A., A. S. Fischer, D. L. Rudnick, C. C. Erikson, T. D. Dickey, J. Marra, C. Fox, and R. Leben, 2002: Moored observations of upper ocean response to the monsoon in the Arabian Sea during 1994–1995. *Deep-Sea Res.,* **49,** 2195–2230.

Wyrtki, K., 1973: An equatorial jet in the Indian Ocean. *Science,* **181,** 262–264.

Xie, P., and P. Arkin, 1997: A 17-year monthly climatology based on gauge observations, satellite estimates, and numerical model outputs. *Bull. Amer. Meteor. Soc.,* **78,** 2539–2558.

Xie, S. P., H. Annamalai, F. Schott, and J. P. McCreary, 2002: Structure and mechanisms of South Indian Ocean climate variability. *J. Climate,* **15,** 864–878.

Yamagata, T., S. K. Behera, J. J. Luo, S. Masson, M. R. Jury, and S. A. Rao, 2004: Coupled ocean–atmosphere variability in the tropical Indian Ocean. *Earth's Climate: The Ocean–Atmosphere Interaction, Geophys. Monogr.,* Vol. 147, Amer. Geophys. Union, 189–212.

Yokoi, T., T. Tozuka, and T. Yamagata, 2009: Seasonal variations of the Seychelles Dome simulated in the CMIP3 models. *J. Phys. Oceanogr.,* **39,** 449–457.